# Piezoelectric Energy Harvesting Utilizing Human Locomotion

A THESIS
SUBMITTED TO THE FACULTY OF THE GRADUATE SCHOOL
OF THE UNIVERSITY OF MINNESOTA
BY

Guojun Wang

IN PARTIAL FULFILLMENT OF THE REQUIREMENTS
FOR THE DEGREE OF
MASTER OF SCIENCE

William P. Robbins

July, 2010

**Acknowledgements**

Thank you Prof. William P. Robbins, for introducing me this is project and offering me a research assistant position. Your direction, guidance and patience throughout my undergraduate and graduate career have been invaluable. I don't know where I would be with your help.

For encouraging me to pursue a graduate degree, thank you Prof. Massoud Amin.

For supporting me throughout my graduate school career and being there for me through the highs and lows, thank you Van.

Thank you Dad, Younlong Wang, for encouraging me to pursue a degree in Electrical Engineering, without you none of this is possible.

## Dedication

This thesis/project is dedicated to my Mom, Jiawei Wang. Your constant love and kindness sustains me now and always.

**Abstract**

Previous studies have shown that not only are piezoelectric materials feasible for energy harvesting, they are feasible as an energy harnessing medium in shoes during walking. Continuing in that vein, this thesis provides new designs to better apply mechanical stress and achieve higher power output. Two points of stress during walking were used for energy harvesting. 1.) The heel of the shoe, for when a person's foot first lands on the ground during the initial stage of the step. 2.) The ball of the shoe, for the curling motioning of the foot as the person propels forward finishing a step.

A flexible, multilayered insole was developed for the ball of the shoe operation and integration into the sole of a specially selected "street shoes". The insole consists of six layers of PVDF sheets, three sheets per side, adhered to a thick but flexible Nylon core. The PVDF absorbs the mechanical compression or tension stress, depending on the side they are on, thereby creating a charge differential across the surface of each sheet. A rigid, reversed clamshell piezoceramic transducer was developed and integrated into the heel of the same shoe. The insert consists of two Thunder PZT unimorph connected in parallel and mounted inside a steel housing to facilitate optimal force transference.

The inherent capacitive property of the piezoelectric materials and its very low frequency of operation (~ 1Hz or 1 step per second), allows for very little current to be extracted

through conventional full-wave rectifier harvesting circuit. Due to previous research success with resonating an inductor in series with the piezoelectric source, an energy harvesting circuit coined "Synchronized Switch Harvesting on Inductor" SSHI was utilized to increase power output. However, due to the inability to correctly synchronize the switching circuit and lack of proper piezoelectric source modeling, SSHI circuit only provided marginal improvement in power output ~10-20% as oppose to previous study demonstrating 250%+ output. Nevertheless, by using only full-wave rectifier harvesting circuits, the new PVDF insole and PZT insert designs have propelled harvestable energy to 11-13mW from one shoe, with a combined generation of 22-26mW for both shoes.

Thesis Supervisor: William P. Robbins

Title: *Piezoelectric Energy Harvesting Utilizing Human Locomotion*

## Table of Contents

## List of Tables

## List of Figures

# CHAPTER 1

# Introduction

The purpose of this work is to develop a piezoelectric energy harvesting system that fits within a pair of shoes for unobtrusive, electrical energy generation from the compression and tension energy normally absorbed by the shoes during walking. Specifically, two shoe inserts were developed, one made of piezoelectric-ceramic unimorph for the heel of the foot and the other made of a six-layer piezoelectric-film for the ball of foot, then a synchronized switch harvesting circuit was investigated to maximize electrical power output. This chapter provides the motivation, background and objectives for this work followed by a brief overview of the remaining report.

## 1.1 Motivation

Personal electronics have proliferated in the past few decades, and consumer demands for decreasing size and increasing mobility underscore a need for new ways of powering these devices. The issue was and has always been of storage and distribution. Traditionally, batteries have been sufficient in both of these roles, but as consumer demand evolves the limitations of batteries will become increasingly incompatible with consumer needs: batteries require regular recharge and replacement due to deterioration, which can be a costly hindrance. A more self sufficient, maintenance free power source is warranted.

Recent advances in ultra-low power electronics have provided opportunities for a new power supply solution: generation and storage of energy at the load by scavenging wasted energy from ambient energy sources, which are renewable and environmentally friendly. The human body is an ideal genesis for such energy scavenging since the load will be close to the source, increasing mobility and decreasing upkeep. The average person spends a significant percentage of their day walking, dissipating a sizable portion of their total energy into the environment. If this wasted energy were harnessed unobtrusively and without affecting the normal motion of the walking body, the resulting scavenged energy could be used in a variety of low powered applications. Exercise monitors, Self-powered emergency beacons or locators, radio frequency identification (RFID) tags, and health monitors are just a few examples of suitable low-powered systems to utilize this supply storage model.

## 1.2 Background

Previous studies utilizing piezoelectric materials for electrical energy harvesting during walking have shown both feasibility and potentiality for energy extraction. More notably, the MIT Media Laboratory has done various feasibility studies of harnessing wasted energy from the human body [1]. One such study from 1995 examined various human activities for possible energy harvesting, and concluded that one of the most

plentiful and readily available energy source is the heel strike during walking [N3]. The study estimated that for an average person weighting approximately 150lb and walking at a brisk pace of two steps per second, 67 Watts of power is available in the heel. Unfortunately, it is impossible to scavenge all of that energy; however, even a small fraction could provide enough electrical power to supply many of the mobile electronics on the market today. A second Media Laboratory study concluded that energy harvesting via walking can be done by embedding piezoelectric materials and control electronics within the shoes [2]. Additionally, because of the large volume and possible available space within a shoe or boot, it provides an environment ideal for the storage of body source energy harvesting instrument.

In addition to these studies, the MIT Media Laboratory has further researched into energy harvesting via walking. Three separate studies involving three different integrated shoe devices were conducted [3][4][5]. One of the devices was a rotary magnetic generator mounted externally under the heel of the foot; although the device generated an impressive 580mW of constant power the device itself is bulky and obtrusive to the movement of users. The second device was a combination of two piezoelectric elements: a flexible, 16-layer PVDF film stave developed for imbedding under the insole along the ball of the foot, and a THUNDER composite PZT unimorph fitted underneath the center of the heel. The PVDF stave produced a constant 1.1mW of power under optimum load

while the PZT unimorph produced a 1.48mW of power. The third study further investigated the THUNDER PZT for application underneath the heel. This study developed a bimorph device which achieved a regulated 1.3mW of continuous power at 3V.

Shoe generated electric energy using thin, flexible sheets of piezoelectric materials has also been researched at the University of Minnesota under the direction of Dr. William P. Robbins. In a former study, the maximum power generated from an 8-layer PVDF insole under the ball of the foot using a full-wave rectifier at matched load was able to generate 0.5mW over an optimized load during normal walking speed of one step per second. A PZT ceramic stack was also experimented with by placing the PTZ stack under preloaded stress via a metal clamp trap; the stress is then relieved and reapplied by the heel of foot striking the sides of metal clamp during walking. Although a very innovative design, the extremely precise machining requirements for this PZT stack design were not achievable with the available manufacturing capabilities of the University. The resulting prototype did not produce any meaningful experimental data.

Piezoelectric materials contain intrinsic capacitance. Therefore, at low excitation frequencies of a walking person (~ 1Hz, 1 step per second), very low current is available due to the high source impedance. Higher output currents and hence more power can be

achieved by utilizing a resonate inductor in conjunction with an intrinsic capacitance, such as that of the piezoelectric materials, thus lowering the source impedance. The capacitance of commercially available piezoelectric materials is in the nano-Farad range; coupled with an extremely low oscillation frequency, it is physically unrealistic to design an inductor with enough inductance to resonate with the piezoelectric capacitance without becoming obstructive to the user.

The solution is a Synchronized Switch Harvesting on Inductor (SSHI) circuit which is used to provide resonance between an inductor and the intrinsic capacitance of the piezoelectric material. The SSHI circuit is based upon the energy harvesting circuit developed in a previous study by Ottmann [6]. In Ottmann's research the circuit, under ideal conditions, was shown to provide four to five times the maximum output power of a conventional full-wave rectifier under ideal conditions. The SSHI circuit was developed by Dustin Morris and William P. Robbins at the University of Minnesota, the circuit has been found to lower the optimum load resistance by a significant amount (an approximate factor of two has been demonstrated). Thus, the SSHI circuit can source several times more power than that of a conventional full-wave rectifier (three to four times as much). A simplified schematic is shown in **Figure 1.1**.

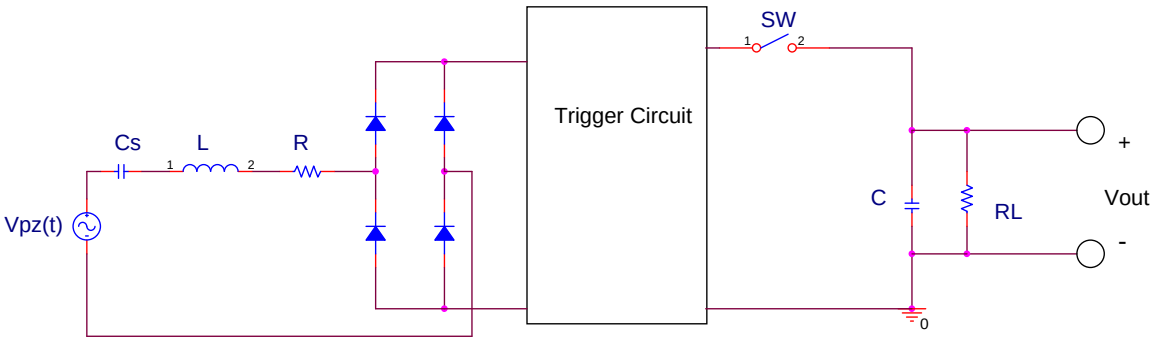


Figure 1.1, simplified circuit diagram of SSHI circuit

## 1.3 Objective

The objective of this thesis is to continue the work outlined above, dramatically increasing the mechanical to electrical power conversion efficiency of piezoelectric materials when subjected to stress caused by the walking foot. The goal is to increase the current accepted maximum output of PVDF and PZT combined power output from 2.7mW to 5mW per foot or to ~10mW per person.

The improvements in power output is achieved by investigating, experimenting and developing innovative electromechinical structures, providing greater strain along the PVDF insole and PZT bimorph. In addition the Synchronized Switch Harvesting on Inductor (SSHI) circuit developed by Morris and Robbins will be investigated and implemented to further increase power output. The SSHI has been previously shown to increase electrical power output by 250%+ [7]. The performance of these piezoelectric

straining structures and the SSSHI implementation will be evaluated and their efficiency compared to the previous design.

The piezoelectric materials power the SSHI circuit; no batteries are needed for initial start-up or to provide a supply voltage to the peak-triggering circuit. A micro-power regulated step-down converter is implemented to provide a 3 Vdc supply voltage to the SSHI circuit. The converter was optimized to have extremely low power dissipation. Therefore, switching frequency was minimized in the design. Filter components such as inductors and capacitors were minimized as well.

### 1.4 Overview

**Chapter 2** discusses the design and electrical characterization of four piezoelectric elements investigated during this project: PVDF, THUNDER PZT, PZT Ceramic Stacks and MFC-PZT. It also provides a basic introduction of piezoelectric theory and terminology and physical operation principles involving various modes of excitation and electromechanical transduction.

**Chapter 3** discusses the overall design of the shoe energy harvesting system. It also details the initial testing for the size and placement of the PVDF under the ball of the foot and the PZT under the heel of the foot. The final placement and size of both piezoelectric

elements are examined and determined for optimum energy harvesting and minimal user interference.

**Chapter 4** outlines the design process of the PVDF insole for the ball of the foot. Material selection, thickness, and shape for the PVDF insole medium is investigated and determined. A progressive improvement of the insole is documented from its initial thin Delrin insole medium to its final, optimum form of thick one side carved Nylon piece. In addition, different adhesives for the PVDF layers are tested and compared for optimum flexibility and maximum stress transfer to the layers. Maximum power measurements are taken for the conventional full-wave rectifier. Then, a brief overview of preliminary experiments as well as initial power measurement is conducted.

**Chapter 5** documents the design process of energy harvesting for heel strike of the foot, utilizing the PZT element. PZT ceramic stacks are revisited; a new electromechanical stressor is designed and analyzed. Ultimately THUNDER PZT is selected as the heel strike element. A bimorph reverse clamshell design is finalized. Maximum power measurements are taken for the conventional full-wave rectifier. Then, a brief overview of preliminary experiments as well as initial power measurement is conducted.

**Chapter 6** explains the operation of the SSSHI circuit including the peak-triggering circuit, switch implementation, and micro-power regulated step-down converter. A specialized inductor is designed for the SSSHI circuit. A brief summary analysis and design of the inductor is given.

**Chapter 7** discusses final implementation and conclusion for this work. It states the best results obtained using piezoelectric materials to harvest walking shoe energy in this research. Final conclusions are drawn; outlining the benefits and shortcomings of current extraction systems, also provides analysis on data collected. Lastly, the chapter concludes by identifying areas of further attention and proposes related future work to increase performance.

# CHAPTER 2

## Piezoelectric Materials

The following chapter provides background theory and overview on various piezoelectric materials investigated and experimented with during this project. It starts with a brief overview of pertinent theory and model of piezoelectric in general. Then, it provides structural and characteristics of the four types of piezoelectric materials investigated in

this project: PVDF, THUNDER PZT, MCF-PZT and PZT Ceramic Stacks. Finally, this chapter presents both the benefits and shortcomings of each of these piezoelectric materials, and provides initial reasoning for material selection for the heel and ball of the foot.

## 2.1 Overview of Piezoelectricity

Piezoelectric materials possess the ability to generate an electric potential in response to an applied mechanical stress (direct piezoelectric effect) and the ability to produce mechanical stress or strain when an electric field is applied (reverse piezoelectric effect). Although the first direct piezoelectric effect was demonstrated in 1880, it wasn't until World War I that the first practical application for piezoelectric materials was developed: sonar. As research progressed, new applications of piezoelectric materials increased drastically over the years. Today, piezoelectric materials are being used in various capacities such as Sensors, Actuators, Frequency standard, Piezo-motors, vibration/noise dampers and now voltage/power sources.

The Piezoelectric effect is present in a wide array of crystalline materials; this effect stems from the asymmetric nature of their unit cell. The unit cell of these materials contains an ion in the center, when mechanical stress is applied to the material; the ions in these unit cells are shifted and irregularly aligned within the crystal lattice. This shift

in alignment creates a charge distribution and subsequent electrostatic potential between the opposite ends of the material (See Figure 2.1). Three factors dictate the relationship between an applied strain and the resulting electric field of a piezoelectric element: the direction of the applied mechanical strain, the size and shape of the element, and the piezoelectric properties of the materials. The various electromechanical *modes* identify the axes of electrical and mechanical excitation is represented by a simple $d_{ij}$-mode notation; the electrical input/output occurs along the *i*th axis, and mechanical input/output occurs along the *j*th (See Figure 2.2). Directions are identified by subscripts 1, 2 and 3, representing the Cartesian coordinates: x, y and z. For example, the $d_{31}$-mode identifies a mechanical strain along the 1 axis, while creating an electric field along the 3 axis; whereas $d_{23}$-mode identifies a mechanical strain along the 3 axis, while creating an electric field along the 2 axis.

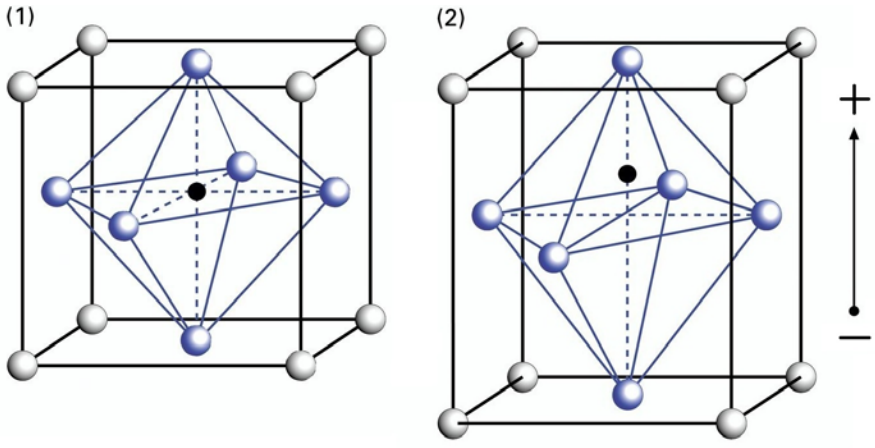


Figure 2.1: Unit Cell of PZT materials with the center ion in black, 1) the material is not electrically or mechanically excited, 2) the material is either mechanically stressed to produce an electric field or is excited by an electric field and physically deformed

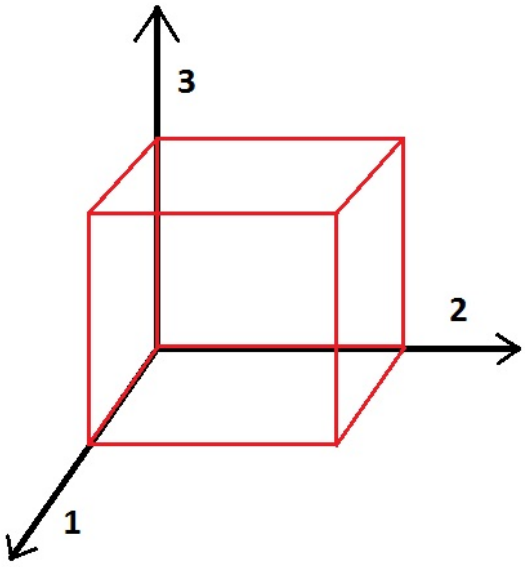


Figure 2.2: Cartesian axis diagram of directional mode of piezoelectric materials.

## 2.2 PVDF Element

The PVDF (Polyvinylidene Fluoride) used in this project is made commercially available by Measurement Specialties Inc. under the product name Metalized Piezo Film Sheets [8]. In addition to two metallization options of silver ink and sputtered metallization, these films are available in many different sizes and thicknesses. The thinner sputtered metallization is more brittle and used where low mass is critical. The silver ink offers excellent flexibility and is ideal for applications where mechanical stress is used. Silver ink metallization is PVDF films are used in this research. The structure and physical dimensions are shown on Figure 2.3 and Table 2.1 below.

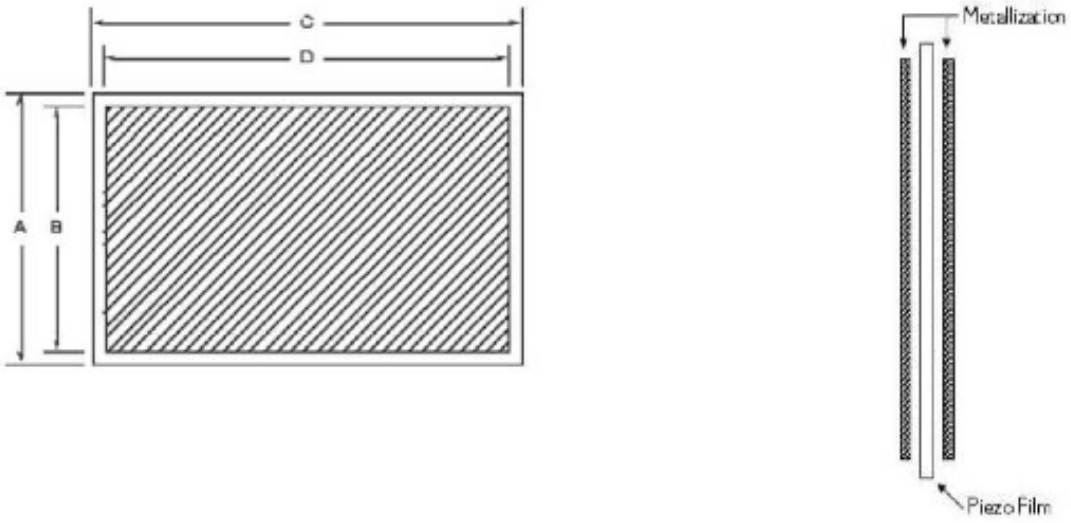


Figure 2.3: PVDF Construction

| | |
|---|---|
| Part Number | 2-1004346-0 |
| Film Thickness | 42um |
| Total Thickness | 54um |
| Metallization | Silver Ink |
| A x C | 203 x 280 mm |
| B x D | 190 x 267 mm |
| Weight | 60g |
| Mode of Operation | d31-mode |
| Capacitance | 100nF |

Table 2.1: PVDF Physical Characteristics

Operating in $d_{31}$-mode these films only provide electrical power when stretched or compressed along the length of the film, therefore application under the heel would require a complex and unnecessary bulky z to x force transfer mechanism. However, the ball of the foot is the ideal location for $d_{31}$-mode operation as foot rotation provides both compression and tension on the shoe insole. Since these film sheets come in such large

sizes: 203x280mm, reduction and sizing are required for custom fitting. This custom fitting requires cutting and bonding the films on to a flexible insole to facilitate $d_{31}$-mode operations. During the custom fitting, the PVDF film's metallization must be removed at the sheet edges by acetone, to insure no short circuiting occurs between the upper and lower surfaces. This is made possible by another unique feature of PVDF; these films are highly non-reactive and pure thermoplastic fluoropolymer making them resistance to solvents, acids, bases and heat. These characteristics are crucial when customizing these PVDF sheets for in-shoe operations, which are detailed in Chapter 3 and 4.

### 2.3 THUNDER PZT Element

Thunder, made commercially available by Face International Corporation, is an acronym for "**TH**in-layer **UN**imorph Ferroelectric **D**riv**ER** and Sensor" [9]. These Thunder elements are based on piezoelectric composite technology originally developed by NASA Langley in conjunction with the RAINBOW (Reduced and Internally Biased Oxide Wafer) design effort [10]. Thunder is a multi-layered ferroelectric device that consists of stainless steel, aluminum and PZT (Lead Zironate Titanate). The different layer materials are tightly bound together using a NASA patented high temperature polyimide adhesive called LaRC$^{TM}$-SI (See Figure 2.3). The manufacturing process consist of precise heating, pressure and cooling cycles resulting in a piezoceramic composite with a characteristic curvature. The curve is due to the Young's modulus of

elasticity of the composite materials, and the different contraction rate of ceramic and metals layers caused by the mismatch in thermal expansion coefficients of the two materials. As the composite cools after heating, the two different materials contract at different rates causing "pre-stressing" and thus curving of the material. When room temperature is reached, stress on the layers within the composite is such that the piezoceramic is in a state of compression while the steel substrate is in a state of tension (See Figure 2.4). Chapter 3 discusses the various Thunder actuator sizes and the selection of TH-6R. (See Table 2.2 for physical dimensions)

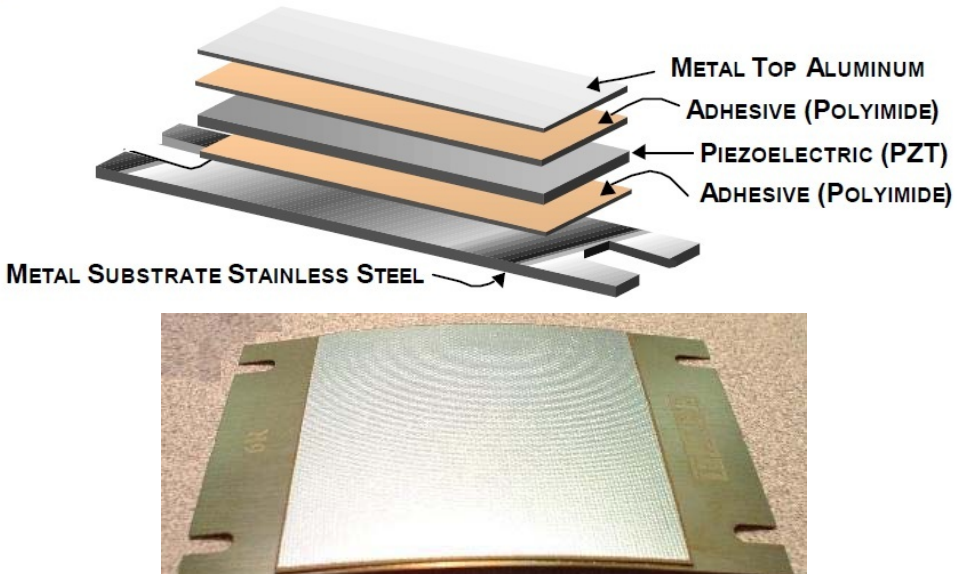


Figure 2.3: Thunder Construction (Top) and actual Thunder TH-6R unit.

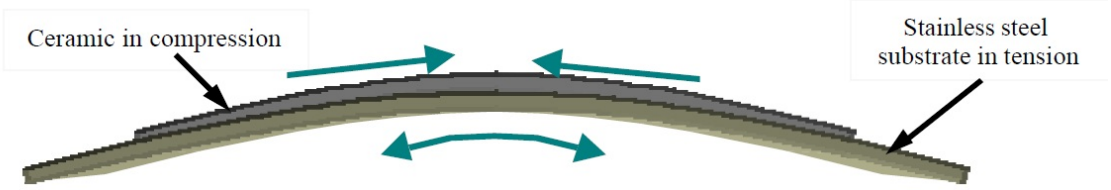


Figure 2.4: Thunder Internal Pre-Stress Conditions.

| Part Number | TH-6R |
|---|---|
| Foot Print (domed) | 75.82 x 51.82 mm |
| Footprint (flat) | 76.20 x 51.82 mm |
| Total Thickness | 0.71mm |
| Piezo Thickness | 0.38 mm |
| Dome Height | 4.24 mm |
| Weight | 16.3g |
| Mode of Operation | d31-mode |
| Capacitance | 75nF |

Table 2.2: Thunder TH-6R Physical Characteristics.

This pre-stress keeps the $d_{31}$-mode piezoceramic in a constant state of compression, which allows Thunder to be deflected far more than standard piezoceramics without cracking or damaged. The pre-stress also yields another unique feature, a natural "pumping" motion, where when the device is flattened it will naturally arch back to the original curved state. These two features make the Thunder an ideal Piezo-element for heel-striking energy extraction, because it can effectively transfer downward force of heel to usable d31-mode stress. In order to protect the actuator from damage and optimize the force transfer a mechanical housing must be designed and implemented to ensure correct operations. This is presented in Chapter 5.

### 2.4 MFC-PZT Element

The MFC (Macro Fiber Composite) PZT experimented with during this project is commercially available from Smart Material Corporation [11]. The MFC consists of

rectangular PZT rods sandwiched between layers of adhesive, electrodes and polyimide film, all in a package no thicker than a few tenths of a millimeter. First developed by NASA in 1996, MFC has been continuously improved and customized to more than 23 standard types now available. The electrodes are attached to the film in an interdigitated pattern which transfers electric potentials directly to and from the ribbon shaped robs (See Figure 2.5). The MFC is available in two significantly different constructions, characteristics and operational modes: P1 Type (d33-mode) and P2 Type (d31-mode) (See Figure 2.6). The P2 Type was the first selected for this experiment, however as Chapter 3 will show, major shorting of the MFC-PZT prevents further investigations on the other type. (See Table 2.3 for physical dimensions)

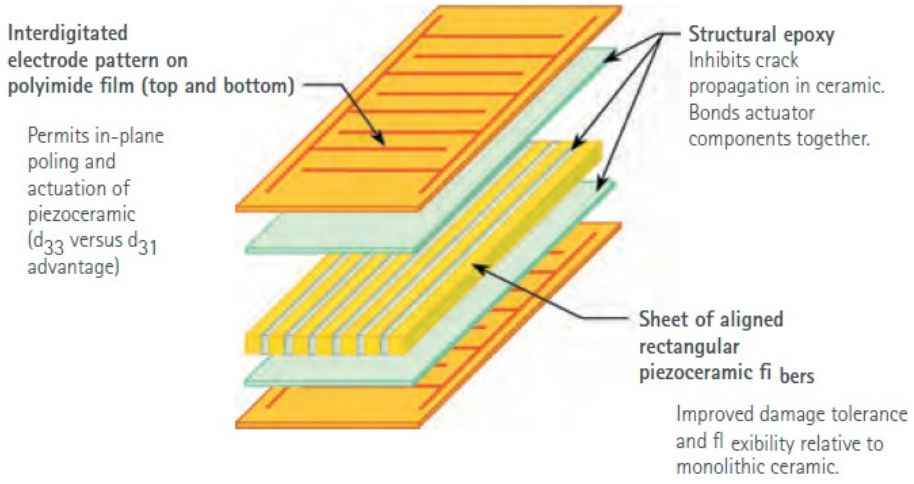


Figure 2.5: MFC-PZT structural construction.

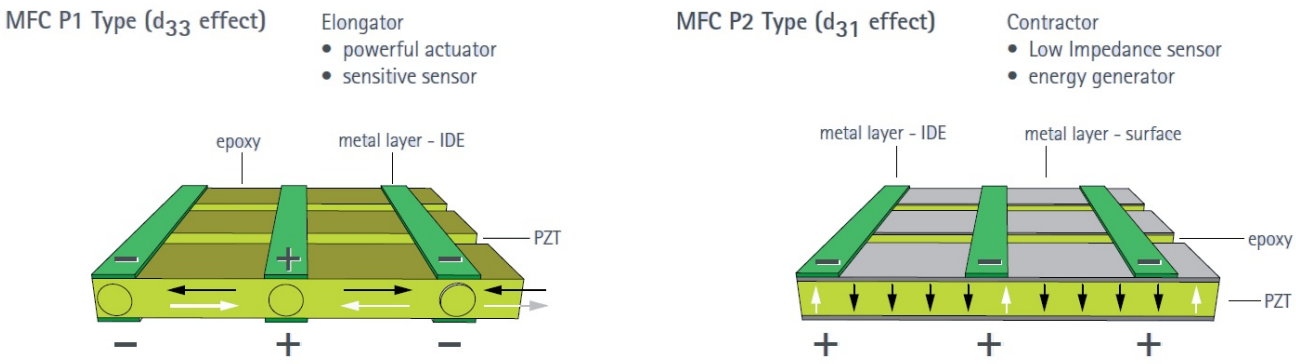


Figure 2.6: P1 Type and P2 Type MFC construction and operation mode.

| Part Number | M-8528-P2 |
|---|---|
| Footprint (Piezo) | 85 x 28 mm |
| Footprint (Overall) | 106 x 34 mm |
| Total Thickness | 0.3 mm |
| Mode of Operation | d31-mode |
| Capacitance | 170nF |

Table 2.3: MFC-PZT M-8528-P2 Physical Characteristics.

Similar to PVDF films, the MFC operates in $d_{31}$-mode making application under the heel prohibitively complex and unnecessarily bulky. Again, the ball of the foot is the ideal location for this kind of $d_{31}$-mode operation. Furthermore, the two types of MFC limit the placement on the insole: P2 Type must be placed on the compress side of insole. Since these sheets come pre-sealed and laminated custom sizing is no longer possible, but M-8528-P2 is small enough in width that two may be place side by side. However, as Chapter 3 will show, this lamination, brittle nature of PZT ceramic fibers and high cost make MFC unsuitable for in the shoe energy harvesting, much less so than PVDF.

.

## 2.5 PZT Stack Element

The PZT stacks used during this project is purchased from American Piezo Ceramics Inc [12]. The stacks are constructed by alternating ceramic and electrode layers during the soft state of the ceramics, followed by a high temperature sintering process that is used to achieve the finished ceramic stack. Two well known stacking concepts have been developed and widely used: "on-stack-insulation" technique (OSI) and "in-stack-insulation" technique (ISI). The OSI-structure exhibit remarkable advantages in actuator performance and ease of handling compared with other techniques. In terms of quantity and diversity of applications the OSI-stacks have the widest distribution at the moment due to their robust and general purpose character. The OSI-stacks are made by fusing a fine glass filament onto the PZT-ceramic stack, where the internal layer electrode comes to surface and shall be separated electrically from the counter-polar supply electrode. The PZT stacks used in this project are OSI-based. (See Figure 2.7 for construction schematic and Figure 2.8 for dimensions diagram and Table 2.4 for physical characteristics.)

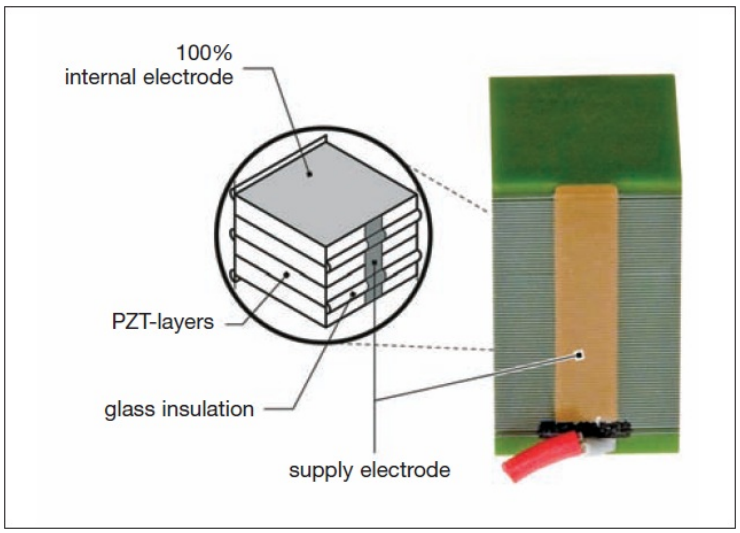

Figure 2.7: Schematic of osi-based PZT ceramic stack construction

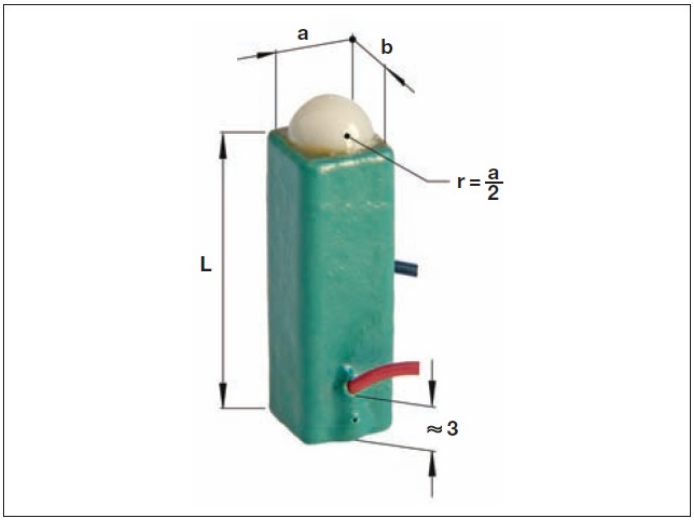

Figure 2.8: Diagram of PZT ceramic stack dimensions

| Part Number | PSt 150/5x5/20 |
|---|---|
| Ceramic Cross-section | 5x5 mm |
| Length (L) | 18 mm |
| Max. Load Force | 2000 N |
| Mode of Operation | d33-mode |
| Capacitance | 1800nF |

Table 2.4: PZT Stacks, PSt 150/5x5/20 Physical Characteristics.

These PZT ceramic stacks operate in $d_{33}$-mode, which make them an ideal candidate for under the heel energy harvesting. However, due to the height of these stacks they cannot be placed under the heel without a mechanical housing to transform downward compression into sideway compression. Although these offer the energy harvesting in a compact packaging, they require a mechanical housing that accomplishes the force transfer without damaging the stacks, which are brittle. These issues are presented in Chapter 5.

# CHAPTER 3

## Initial Testing and Design

This chapter provides a system overview of the shoe energy harvester, detailing the various components of this system and their functions. Optimum operation modes of the piezoelectric materials for the shoe energy harvesting, and placement of piezoelectric materials are discussed. Initial testing for optimal dimension and placement of PVDF/MFC under the ball of the foot, and PZTs under the heel of the foot are conducted. The final placement and dimension of both piezoelectric elements are determined for optimum energy harvesting and minimal user interference.

### 3.1 System Overview

The energy harvesting shoe system is conceptualized as harvesting energy from two points of contact during normal walking. (See Figure 3.1) The first point is the "Contact Phase", which occurs when the heel strikes during foot landing; vast amounts of energy are absorbed by the insole of shoe through compression of the material. The second point is the "Propulsive Phase", which occurs when the ball of the foot bends after landing followed by pushing off at the tip of the shoe to propel the person forward.. Energy here is also absorbed by the insole of the shoe through bending the material. The system consists of placing two piezoelectric energy harvesters at those two critical points for energy extraction. The two Piezo-elements are vastly different from each other since their modes of operation are differed by vertical compression and horizontal tension/compression. Therefore, two varieties of housing and mechanical apparatus are required to ensure proper force placement and protection of the Piezo materials. The final piece of the system is an extraction circuit which will maximize power extraction and provide energy storage. (See Figure 3.4 for complete system diagram)


Figure 3.1: Foot Phases descriptions during normal walking.

One of the important selections of the design is the shoe. In previous studies boots and athletics shoes are used [1], although practical and utilitarian, these shoes exhibit one major flaw when harnessing "Propulsive Phase" energy; they inherently have manufactured lift at the tip of the toe. (See Figure 3.2) This lift causes a internal curve within the shoes that reduces the bending motion during the "Propulsive Phase" thus reducing mechanical strain on the Piezo-elements minimizing power extraction. After analyzing various shoe types, urban/street shoes were select as the shoes of choice for their flat bottoms. The power elicited by the bending during the "Propulsive Phase" is then maximized.

Figure 3.2: Athletics Shoes and Boots with Prominent “Toe Lift”

Figure 3.3: Street Shoe with Flat Toe and Bending During Propulsive Phase

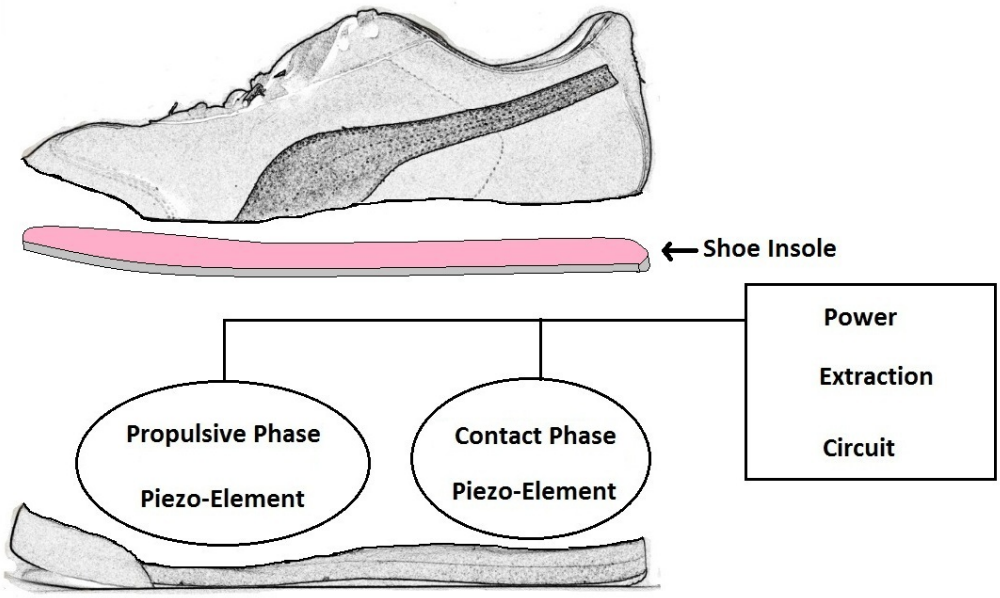


Figure 3.4: Piezoelectric Shoe Energy Harvester System Diagram

Another important design decision was to keep the Piezo-Element non-intrusive and comfortable for users. For "Contact Phase" Piezo-Element, this means the design will strive to maintain the cushioning property of shoe, while keeping the thickness to a minimum. For "Propulsive Phase" Piezo-Element, this means the design will strive to maintain the flexibility, while keeping the oversize and thickness to a minimum. These design goals will be revisited and used as a guideline throughout this project; furthermore it will be a prominent feature in the following two chapters.

### 3.2 Piezo-Element Operation Mode, Placement and Sizing

The "Propulsive Phase" Piezo-Element is envisioned to be an insole like material with a medium substrate that will facilitate the stress transfer. (See Figure 3.5) First

PVDF orientation placement and size must be determined. This is accomplished by using small strips of PVDF materials, glued onto a thin plastic substrate using 3M double sided tape and placed within the shoe for stress samples. Electrodes were attached to the opposite surfaces and electrical performance samples of d31-mode PVDF were measured with an oscilloscope.

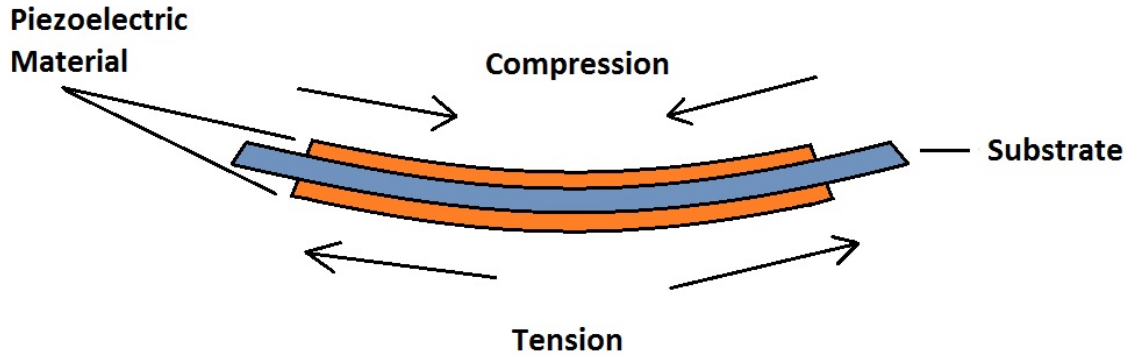


Figure 3.5: Stress Diagram for "Propulsive Phase" Piezo-Element

The first test was to size the substrate width. This test was done by placing four strips of PVDF materials side by side length-wise across the width of the of a test substrate. Each PVDF strip was the same width and length: 1.5 x 8.5cm. Since they were of the same materials each have near identical intrinsic capacitance of 3.10nF. (See Figure 3.6) Electrodes were attached to all four PVDF strips then placed within the shoe for oscilloscope measurement. In Figure 3.7, the voltages across all four PVDF strips during one step were recorded and presented. These identical properties were used to determine if any one area along the width of the Piezo-shoe insert was being stressed more than the rest. If such stress variations do exist, the dimensions of the PVDF

materials can be adjusted accordingly to maximize power extraction. The hypothesis was that since the medium substrate material, Delrin, was relatively rigid and it was being bent length-wise, there should not be any significant stress gradient across the width of the material.

Figure 3.6: PVDF Insole Strip Test for Optimum Width

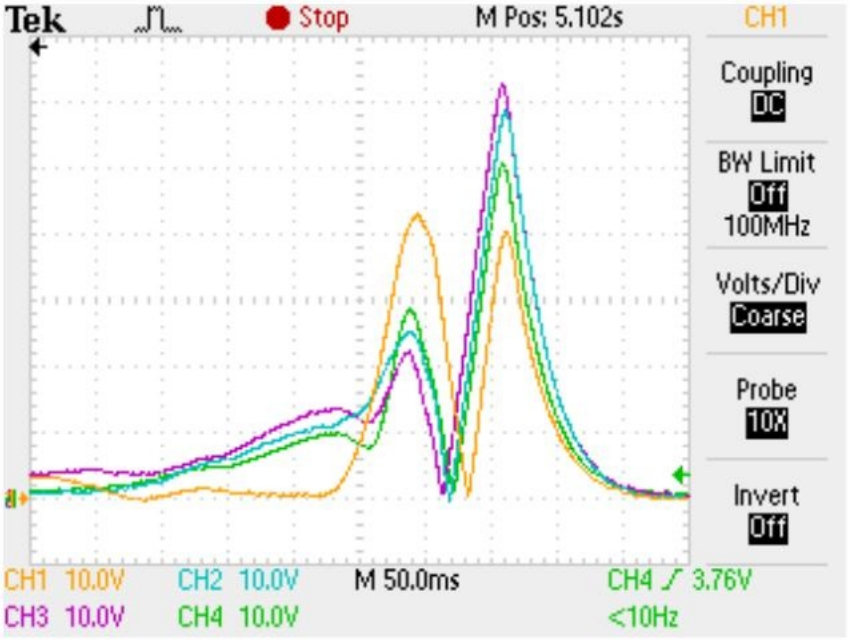


Figure 3.7: Voltage Measurement for Optimum Width, Channels Correspond to Figure 2.6

Results in Figure 3.7 validated this hypothesis, showing that the materials were getting about the same amount of stress across the insole substrate. This relatively uniform stress application across the substrate was due to minimum flex between the PVDF strips or minimum flex along the width of the substrate. From this experiment, it was evident that the width of the PVDF sheet can be as wide as needed, since there is no significant difference in the applied stress across the width of the insole core.

The second test was to size the substrate length. This test was done by placing three pieces of PVDF materials in a column along the length of a test substrate. Each PVDF strip is the same width and length: 6.0 x 4.5cm. Again, since they are of the same

materials each have near identical intrinsic capacitance of 6.5nF. (See Figure 3.8) Finally, electrodes are attached to all four PVDF strips were then placed within the shoe for oscilloscope measurement. In Figure 3.9, the voltages across all three PVDF strips during one step were recorded and presented. This experiment was to determine if a stress gradient exists along the length of the substrate. The hypothesis here is that since the medium substrate material is being bended length-wise, there should be a high stress area on the substrate right where the ball of the foot should be (CH2).

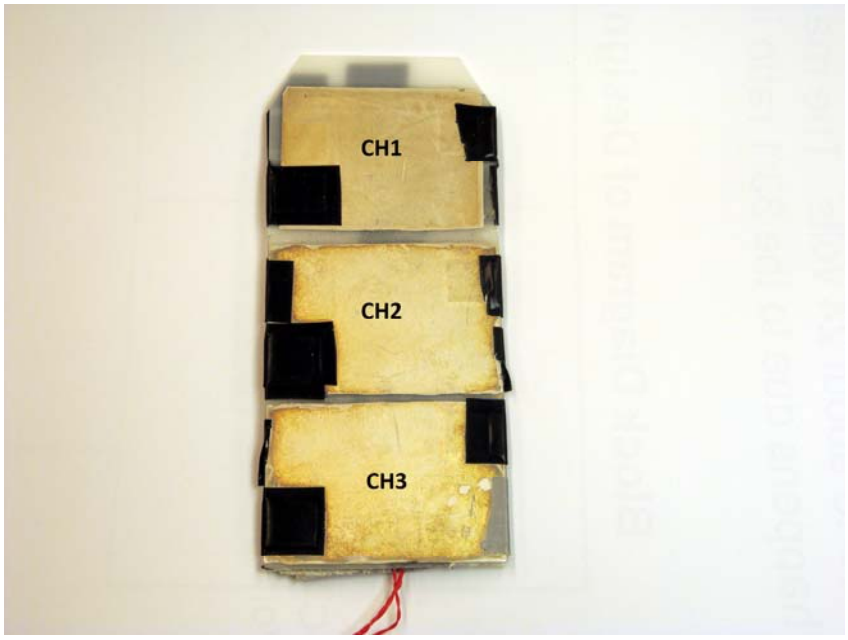

Figure 3.8: PVDF Insole Strip Test for Optimum Length

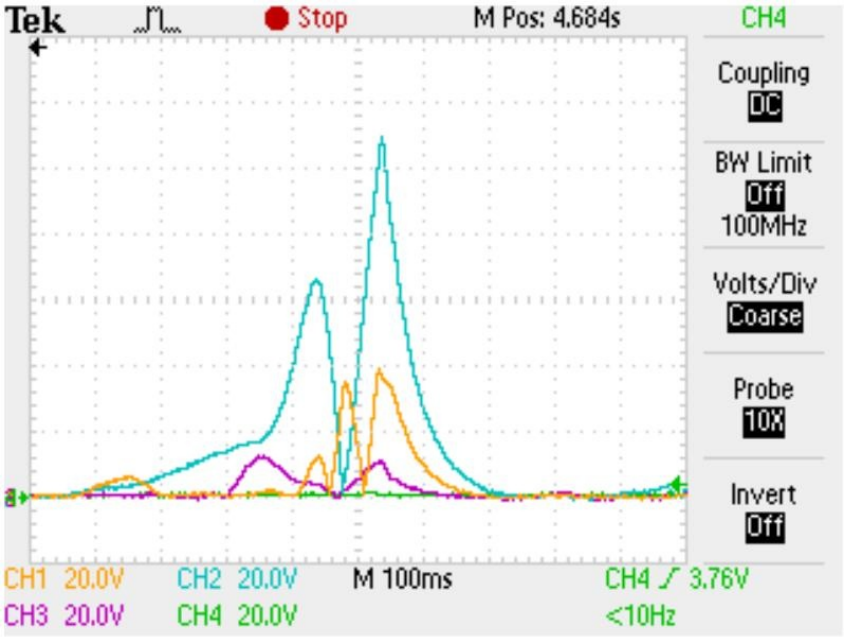


Figure 3.9: Voltage Measurement for Optimum Length, Channel Correspond to Figure 2.8

Results in Figure 3.9 validated this hypothesis, showing that the highest stressed area was right around the ball of the foot, as denoted by CH2, with peaks over twice as high as all other areas. It is interesting to note that the other two areas are not being stress much, if at all, therefore not contributing to any energy conversion. From this experiment, it was determined that the length of the Piezoelectric material should be focused along the ball of the foot, any length longer than this area would not contribute toward stress to electrical transfer. Additionally, another critical design point of the PVDF materials is the direct correlation between intrinsic capacitance and volume. A higher capacitance will result in lower optimum load impedance for power extraction, which in turn simplifies the extraction circuit design and reduces component

requirements. Therefore, the substrate size must take all factors in to account: stress gradient along the width and length of the insole substrate, PVDF materials cost, PVDF volume/capacitance relationship, and available shoe space for the insole (See Figure 3.13). The final insole size for the "Propulsive Phase" was determined to be 7.0x14.5cm. (See Figure 3.10) This design was set for the rest of this project and all other developments on the "Propulsive Phase" insole do not change these dimensions. From the figure another feature of the substrate is the lack of two top corners; these are cut off so that the insole may slide further up the shoe towards to toe, thus placing the ball of the foot at the middle of Piezo active region. The additional space at the bottom of the substrate was to provide room for electrode attachments, without which, the electrode are easily damaged or destroyed during usage.

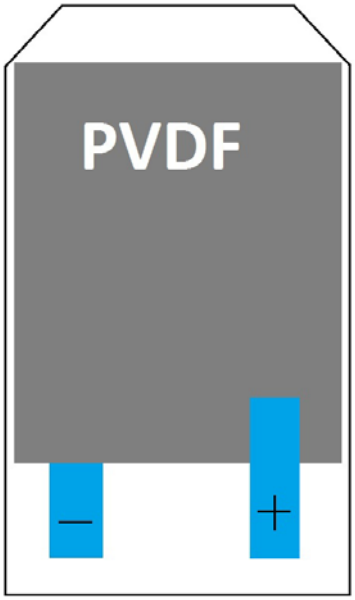


Figure 3.10: "Propulsive Phase" Insole Surface Design

Next, initial testing with MFC-PZT was conducted to identify both the optimum placement and number of pieces. Similar to the PVDF tests, a piece of MFC was glued using 3M double sided tape onto a thin plastic substrate. Resulting oscilloscope readings are shown on Figure 3.11. Although the voltages were much lower than the initial PVDF testing, MFC has a much higher capacitance thus resulting in a much lower matching load resistance. Further testing MFC could very well be a viable alternative to PVDF.

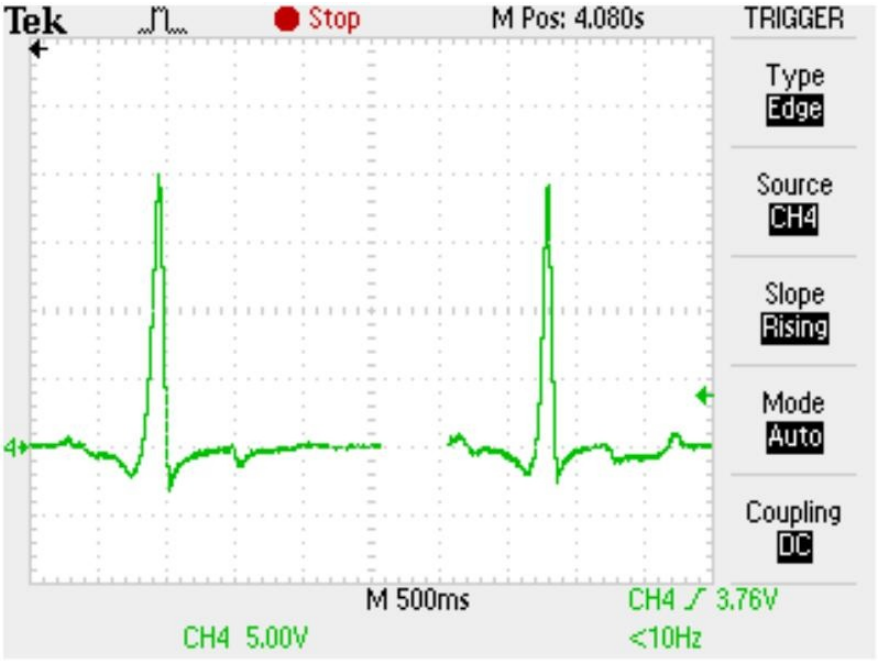


Figure 3.11: Voltage Measurement for Initial MFC-PZT Testing

During testing the MFC piece had to be moved across the plastic substrate to determine optimum location. It was quickly apparent the brittle PZT fibers within the

MFC could not handle the stress required from the moves. Tiny, unnoticeable cracks resulting from testing stress caused critical damage when their growth was aggravated by continuous testing to the point of severing one of the electrodes and cutting almost completely across the MFC. This issue was compounded by the high cost of these MFCs, which makes any permanent glue testing of these materials prohibitively expensive. Therefore, MFCs were not considered for further study and the "Propulsive Phase" Piezo-element was developed with PVDF only.

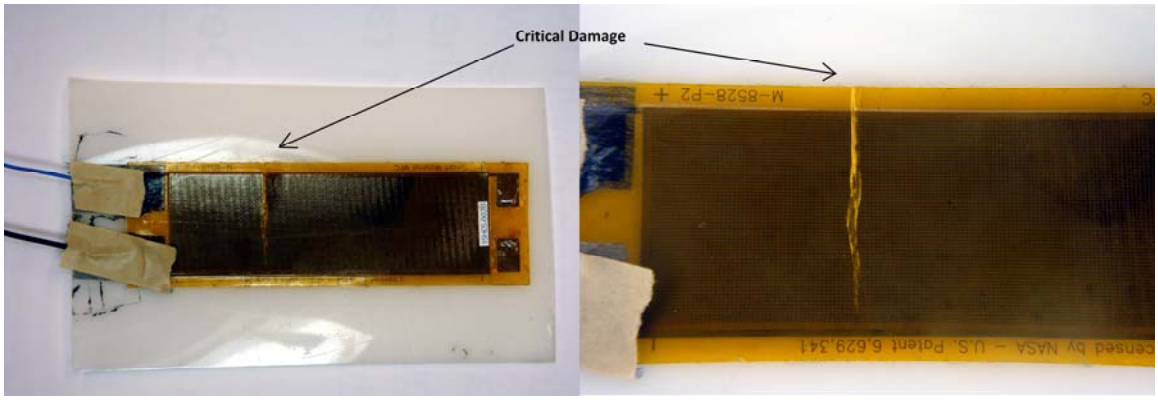

Figure 3.12: MFC-PZT Initial Placement Test

Finally, the "Contact Phase" Piezo-element was envisioned to be centered squarely on the heel of the foot. This leaves two design limitations on the element: overall width and length, which was determined by the size of the shoe heel, and the height of the element, which was also determined by the shoe heel. From measurements on Figure 3.13, the maximum space for the element was determined to be 6.5x8.5x2cm. Both the PZT stack and TH-6R fall well within the size limit, however the housing and

force transfer apparatus required for proper operation needs additional space. These factors and detailed design for “Contact Phase” Piezo-element are presented in Chapter 5.

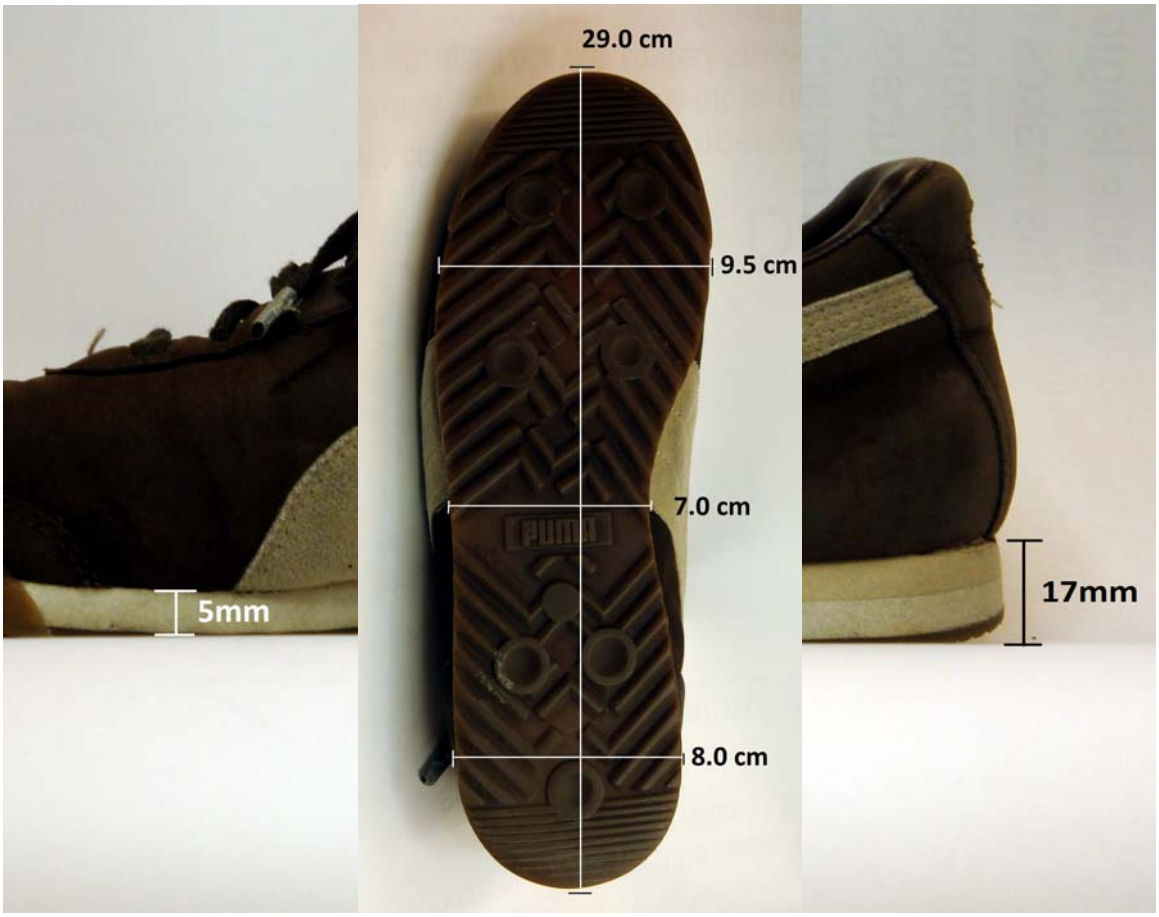

Figure 3.13: Operational Space for Piezoelectric Materials

# CHAPTER 4

**Propulsive Phase Piezoelectric Insole Design**

The shoe's insole dimensions, while flat hence two-dimensional, dictate the limits of the piezoelectric element used during the "propulsive phase" of walking. . These limitations make piezoelectric elements operating in 31-mode, simultaneously thin and flat sheet materials, the most appropriate for insole energy harvesting. In this chapter, PVDF materials are integrated into an insole plate, which are then mechanically excited by flexing the plate about its neutral axis; inducing tension and compression at the insole plate surface. The design process and progression are detailed bellow, with focus on maximum flexibility and power output.

## 4.1 Delrin Thin Insole

The first insole design was based on previous MIT and UofM insole models, using on hand in lab materials and adhesives. The goal was to reproduce established power measurements and expand upon this with design improvements. The insole core is made of a 1.05mm Delrin cut to shape as described on Figure 3.10, and PVDF sheets adhered with 3M double sided tape. The PVDF sheets were also cut and sized to fit on the insole surface. As specified from Table 2.1, each PVDF sheet has an active region of 19.0cm x 26.7cm. Taking high PVDF cost and insole core dimensions into account, each PVDF sheet was cut into nine equal pieces of 6.3cm x 8.9cm. This dimension is standard

for all other Propulsive Phase PVDF insoles that follow. Because of silver metallization on PVDF, each cut edge was cleaned with acetone to remove left over silver in order to prevent short circuiting of two surfaces. Four sheets were adhered to each side of the insole core, resulting in an 8-layer construction. (See Figure 4.1)

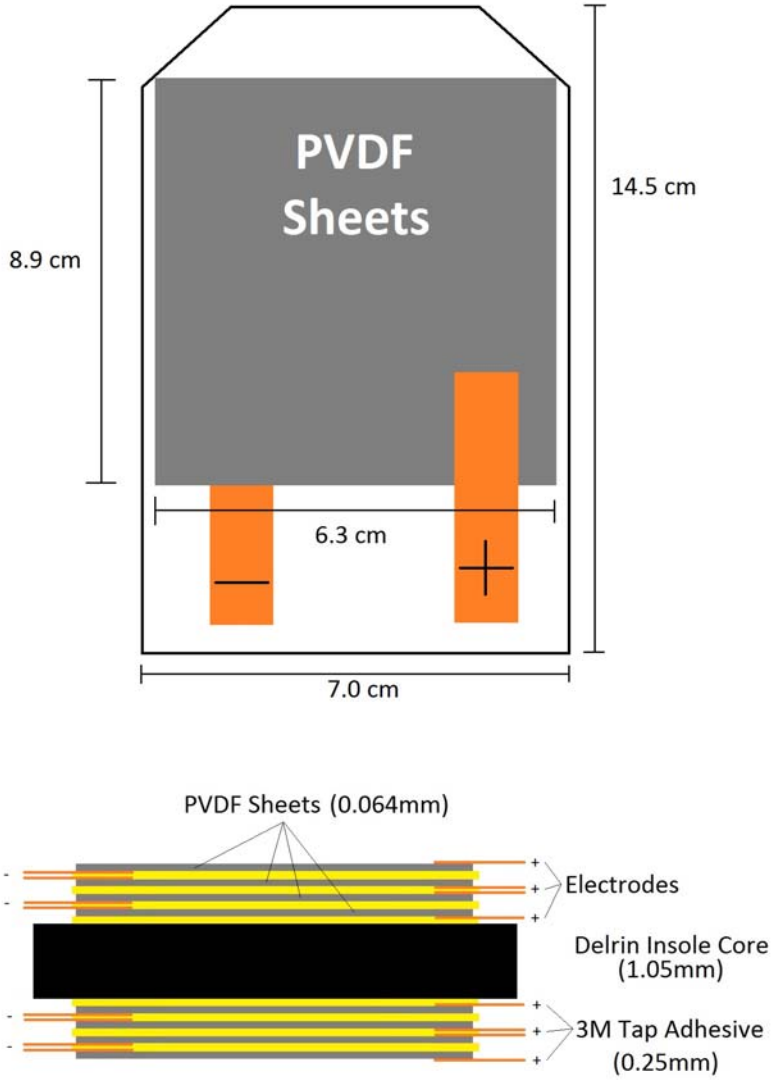


Figure 4.1: Propulsive Phase Delrin Insole Diagram

$$C_{PVDF} = \varepsilon_0 \varepsilon_R \left( \frac{A}{d} \right) \qquad \text{(Equation 4.1)}$$

$$C_{PVDF} = (8.85x10^{-12} F/M)(11)\left( \frac{513cm^2}{.005cm} \right) = 100nF \qquad \text{(Equation 4.2)}$$

Each PVDF sheet has an intrinsic capacitance described by equation 4.1, with $\varepsilon_o$ being the permittivity of free space, $\varepsilon_r$ the relative permittivity of PVDF, *A* the active area of PVDF, and *d* as the thickness of the PVDF. Equation 4.2 presents the actual capacitance of each custom cut PVDF sheet: 10.1nF, which is also experimentally verified by a RLC multimeter. Each of these PVDF sheets are then connected in parallel by the arrangement of electrodes, therefore through parallel combination the total capacitance of the insole, ~80nF, is the sum of each layer. The open-circuit voltage is, then, the average of each layer due to the fact that the further away the PVDF sheet is to the surface of the insole the more strain is applied resulting in higher voltages. Another issue that arose was the combination of tension and compression layers, from experimental results the compression open source voltages were lower than tension source voltages. (This issue is further discussed in section 4.2) As observed from Chapter 3, figure 3.8 and 3.9, the piezoelectric elements under the stress of each step creates a pulse voltage with relatively constant amplitude, which can be modeled by a pulse voltage source in series with a capacitor. (See Figure 4.2)

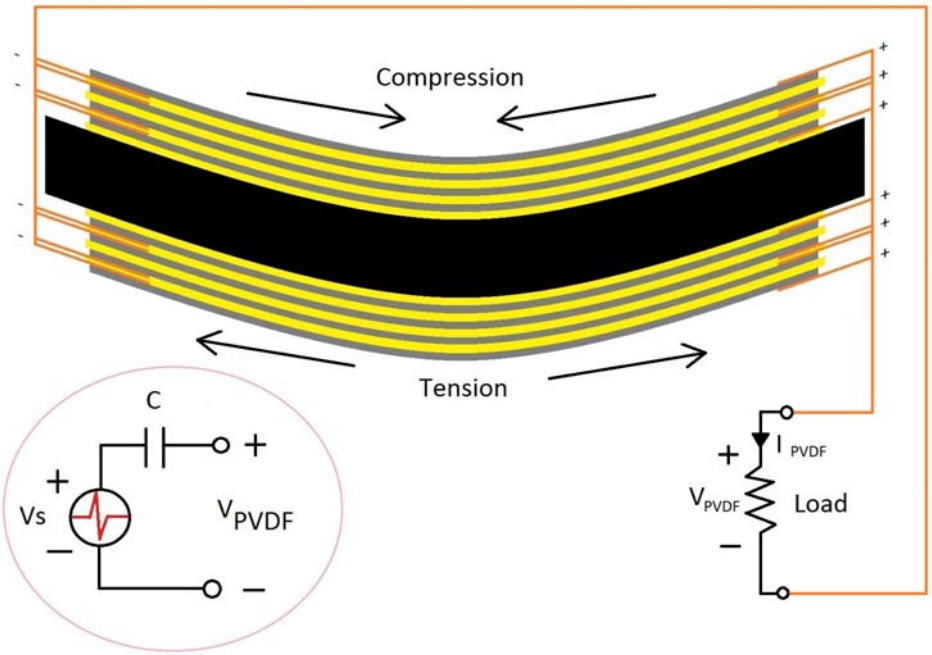


Figure 4.2: PVDF Propulsive Phase electrical connection diagram and equivalent circuit.

$$R_{Optimal-Load} = \frac{T_s}{4C_s} \qquad \text{(Equation 4.3)}$$

Power measurement was conducted by placing the insole under the shoes and implemented during walking while connected to a full wave rectifier and a multimeter to keep measurement. (See Figure 4.3) The optimal resistance was first estimated via equation 4.3, where *Ts* is the time of each step, and *Cs* is the source capacitance of Piezo insole. For the eight-layer insole, the Cs is 80nF and Ts is set at one 1 for one step per second, resulting in $R_{Load}$ as 3.125MΩ. Then a set of other load resistances were also

measured at both ends of optimal resistance to insure both power curve was captured correctly and equation 4.3 is applicable for this circuit. (See Figure 4.4)

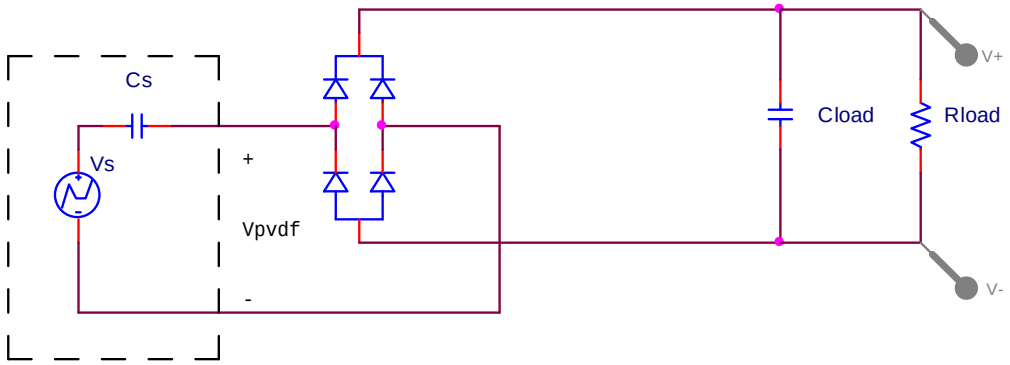


Figure 4.3: Power Extraction Circuit Diagram for Delrin PVDF Insole

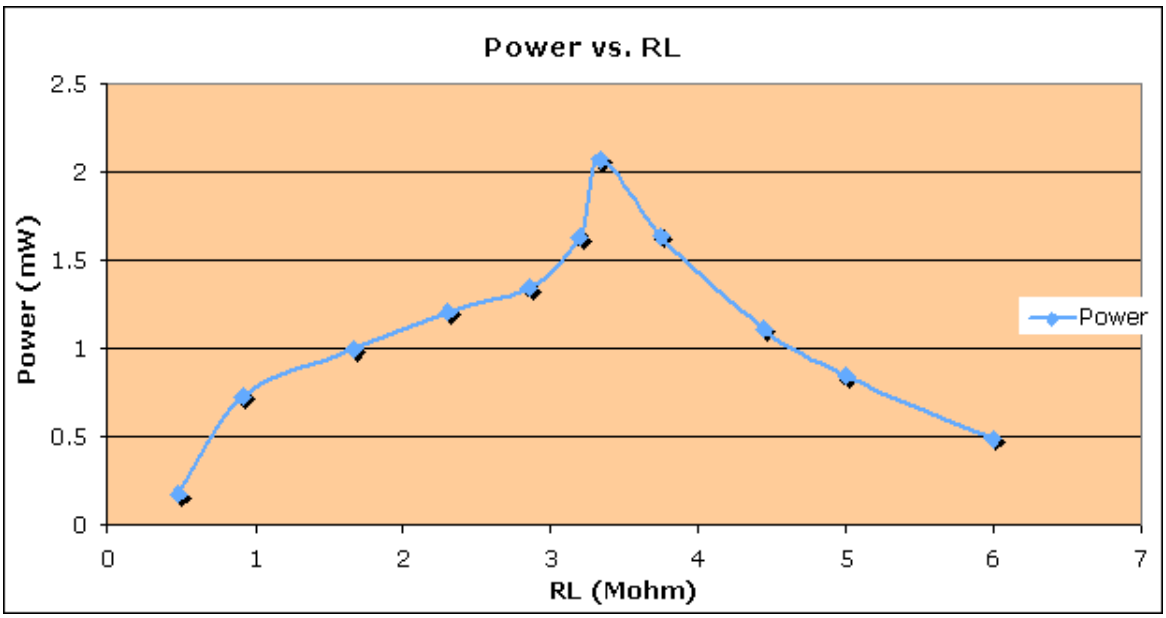


Figure 4.4: Power vs. Load Resistance for the Eight-Layer Insole.

With an optimal load resistance of 3.125MΩ, maximum power extracted with the full wave rectifier is 2.07mW. Although this initial design's power output is impressive,

double of the maximum output from the MIT study [3], the following sections will detail additional (alternative) improvements to further increase power output.

### 4.2 Compression and Tension Voltage Output Issue

A complication that arose during experimentations with the Delrin PVDF insole involved production of voltage power even though the two sides of the bimorph consist of the same material, adhesive, and distance from the neutral axis. The compression side peak amplitude voltages comprise about 50%-60% of tension side peak voltages. When placed in parallel the output voltages across the load is the average of two source voltages. (See Figure 4.5) The power voltages and capacitances can be used in the equations denoted below to calculate the lowest peak amplitude possible before the compression side becomes parasitic and consequently decrease the overall power output. The compression side can be taken out completely to avoid this issue; however, with each additional layer more capacitance is added and thus reduces optimal load resistance. The other option would be to add all the layers on the tension side of insole, but with each additional layer added to the tension side the neutral axis of the insole bend moves closer to the PVDF sheet sides. This shift of neutral axis reduces stress on the tension sheets thus presents the same issue as that of the compression and tension voltage output differences.

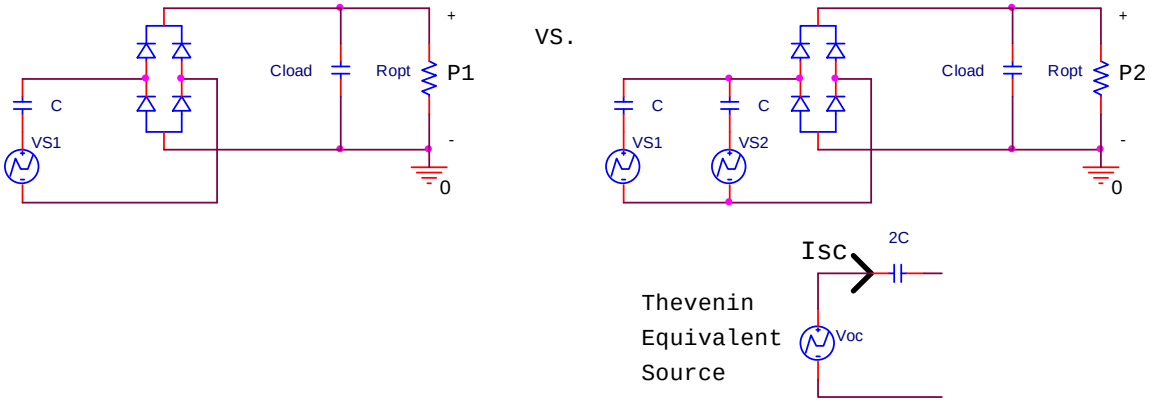


Figure 4.5: Circuit Diagrams of Single PVDF Sheet Vs Dual PVDF Sheets

For single PVDF Sheet:

$$P_{MAX} = \left(V_s/2\right)^2 \times \frac{1}{R_{opt}} = \left(V_{s1}/2\right)^2 \times \frac{4C}{T} = \underline{\frac{V_{S1}^2 C}{T}} \qquad \text{(Equation 4.4)}$$

For Dual PVDF Sheets:

$$V_{OC} = \frac{(V_{S1} - V_{S2}) \times 3C}{2} \times \frac{1}{3C} + V_{S2} = \underline{\frac{V_{S1} + V_{S2}}{2}} \qquad \text{(Equation 4.5)}$$

$$I_{SC} = V_1 SC + V_2 SC = \underline{(V_1 + V_2)SC} \qquad \text{(Equation 4.6)}$$

$$\frac{V_{OC}}{I_{SC}} = \frac{(V_{S1} + V_{S2})}{2 \times (V_{S1} + V_{S2})SC} = \underline{\frac{1}{2SC}} \qquad \text{(Equation 4.7)}$$

Thevenin Equivalent Source Capacitance calculated to 2C.

$$P_{MAX} = \left(\frac{V_{OC}}{2}\right)^2 \times \frac{1}{R_{opt}} = \left(\frac{[V_{S1} - V_{S2}]/2}{2}\right)^2 \times \frac{4 \times (2C)}{T} \qquad \text{(Equation 4.8)}$$

$$= \left(\frac{V_{S1} - V_{S2}}{4}\right)^2 \times \frac{8C}{T} = \underline{\frac{(V_{S1} - V_{S2})^2 \times C}{2T}}$$

Maximum power output of Dual PVDF sheets must be higher than Single PVDF sheet for

$$\frac{V_{S1}^2 C}{T} < \frac{(V_{S1} - V_{S2})^2 \times C}{2T} \qquad \text{(Equation 4.9)}$$

$$V_{S1}^2 < \frac{(V_{S1} - V_{S2})^2}{2} \Leftrightarrow V_{S1} < \frac{V_{S1} - V_{S2}}{\sqrt{2}} \Leftrightarrow \sqrt{2} < 1 - \frac{V_{S2}}{V_{S1}}$$
$$\Leftrightarrow \frac{V_{S2}}{V_{S1}} < 1 - \sqrt{2} \Leftrightarrow V_{S2} < (-0.414) V_{S1} \Leftrightarrow \underline{V_{S2} > 0.414 V_{S1}} \qquad \text{(Equation 4.10)}$$

Equations 4.4 – 4.10 show that given two voltages in parallel with two capacitors such as those in sources like that of PVDF, the minimum voltage of the second voltage source (Vs2, Compression Side) must be above 41.4% of first voltage source (Vs1, Tension side) so that the overall power output of two voltage sources combined is above the single voltage source. As aforementioned the compression side voltage is 50%-60% of the tension side, thus the compression side is contributing to the overall power output. This was continuously checked by measuring the power supply of each side and comparing to measurements of when they are combined. Each time the comparison was done, the power output of combined sides is above the sum of individual sides.

### 4.3 Solid Nylon Insole

The next step to increasing the power output of the PVDF insole was to increase the thickness of the core materials. As briefly mentioned in Section 4.2, as the thickness of core material increases, the PVDF sheets shift further away from the neutral axis of

bend. When the bending angles are the same, this increased in distance away from the neutral axis creates a larger arc providing more mechanical stress for energy conversion. (See Figure 4.6) After consulting with the Electrical Engineering department's machine shop, nylon was determined as the next ideal material to utilize in place of Delrin. Nylon was chosen for its higher durability, elongation, abrasion resistance, resilience, and malleability over Delrin. A 2.34mm thick piece of nylon was used, doubling the thickness of insole core from the 1.05mm thick Delrin from the previous experiment. As diagrammed in Figure 4.1, the nylon piece was cut to shape, and then adhered with four sheets of PVDF on both sides. (See Figure 4.7 for resulting insole) The same power extraction circuit as the Delrin insole was used (Figure 4.3).

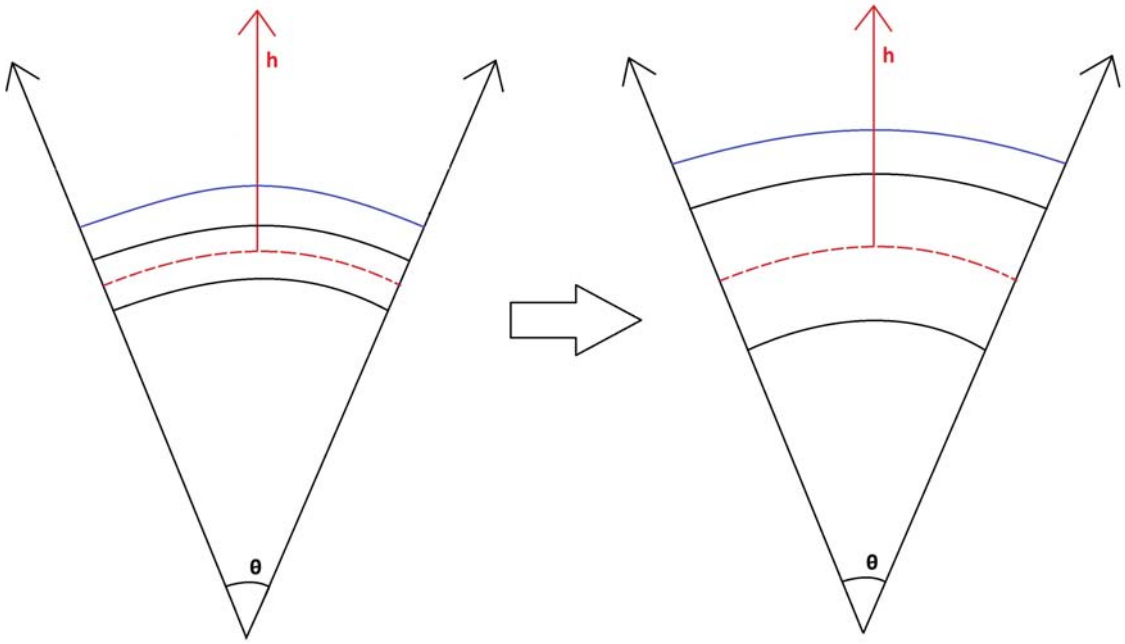


Figure 4.6: Arc Diagram for Change in Thickness

Figure 4.7: 8-layer PVDF Nylon Insole with 3M Double Sided Tape as Adhesive

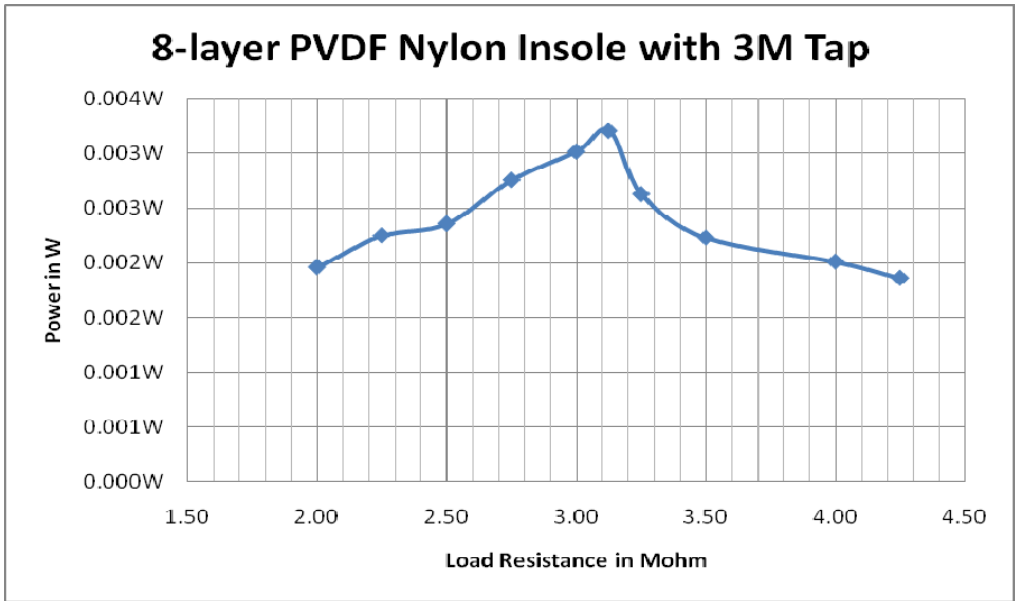


Figure 4.8: Power Curve for 8-layer PVDF Nylon Insole with 3M Tap Adhesive, with maximum at 3.124MΩ and 3.21mW

Since this new Nylon insole has the same source capacitance, the optimal load resistance stays the same at 3.125MΩ (as shown in Equation 4.3). The maximum power extracted at the optimal load was measured to be 3.21mW (see Figure 4.8 for Power Curve), a 50% increase in power output. These experimental results validate that

increasing insole thickness consequentially increases stress/power output. They also further solidify Equation 4.3 as the estimator for optimal load resistance. These findings were used for further insole power output improvement demonstrated in the following section.

The adhesive compound is another component considered for the improvement of the insole. The 0.25mm 3M tapes was used for its ready availability and ease of use, however, the peel strength of these tapes is very week the compression or tension force is not completely transferred to PVDF. The ideal adhesive characteristics sought after are flexibility, high peel strength, and ease of use. Various adhesives were examined and tested by bonding transparent films to a nylon block. Transparent films were chosen because of their similarity in thickness and composition to PVDFs, and most importantly their economy. Each adhesive bond was peel and flex tested, in addition to having their durability examined. After numerous tests, the 3M DP-105 epoxy was determined to be the best choice; it was the most flexible adhesive tested that maintained high peel strength and durability. A piece of the nylon was cut into shape as diagrammed in Figure 4.1, then adhered with four sheets of PVDF on both sides. (See Figure 4.9 for resulting insole) The same power extraction circuit as the previous two insoles was used (Figure 4.3).

Figure 4.9: 8-layer PVDF Nylon Insole with 3M DP-105

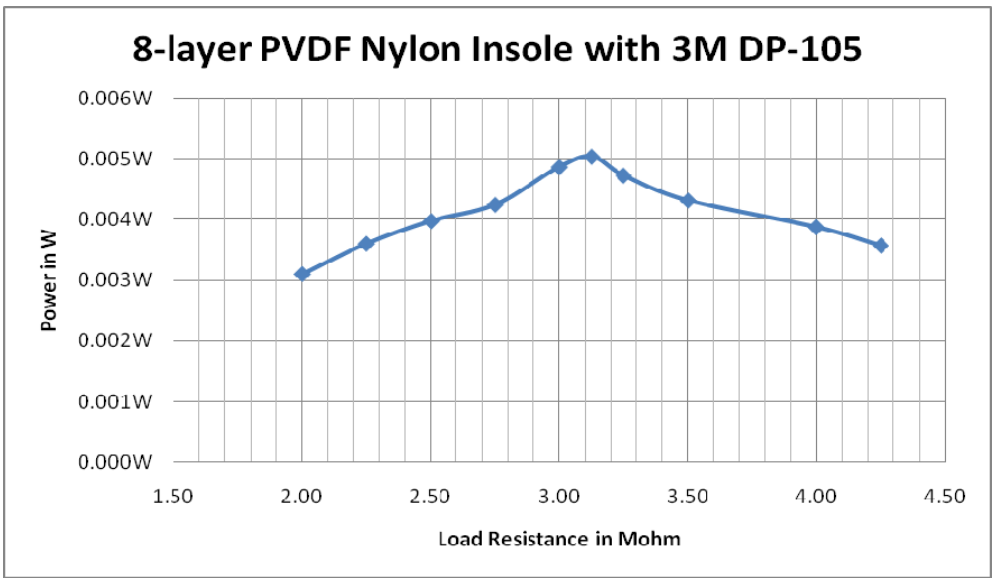


Figure 4.10: Power Curve for 8-layer PVDF Nylon Insole with 3M DP-105, with maximum at 3.125MΩ and 5.04mW.

Again with the optimal load resistance of 3.125MΩ (as shown in Equation 4.3), the maximum power extracted at the optimal load was measured at 5.04mW (see Figure

4.10 for Power Curve). An impressive 57% increase in power output over 3M Tape Adhesive and 143% increase over the thinner Delrin insole, just by switching to 3M epoxy as the adhesive and to nylon as the insole, respectively. However, with the thicker insole core and adhesive improvements another issue surfaced; the insole became too stiff impeding the user's ball of foot movement during walking. The user feels noticeable discomfort on the ball of the foot and excessive strain on the hamstring muscles. This problem prohibited any additional increase in thickness to further increase power output. The next section discusses the final improvements to the insole that alleviates this problem.

### 4.4 Etched Nylon Insole

Although various methods for increasing flexibility while preserving thickness were explored one method stood out the most, etching the insole. The idea initially came from examining the construction of a cardboard box, where its thickness is due to its hollowed midsection structure. The insole core was envisioned as an inside out cardboard box. The surface of the insole was etched so that its exterior structure mimics that of a cardboard box's interior structure (See Figure 4.11 and 4.12). The insole core was etched widthwise as oppose to lengthwise or hollowed because neither improved flexibility. From trial and error, the substrate midsection was etched down to 0.78mm (30mils) to achieve similar flexibility of a Delrin core which did not produce any

discomfort nor impede the movement of the user. Etching thinner than specified may run the risk of the substrate easily taking a permanent "shape" after a prolonged period of bending; any thicker then the substrate's flexibility may be compromised. Due to this construction additional thickness can be obtained without sacrificing flexibility, as long as the mid section is kept at 0.78mm. A final thickness of 3.22mm (127mils) was selected for its ideal balance of flexibility and shock absorbency. Any further increase in thickness would reduce the shoe's shock absorbency, as further cutting of the 5mm high shoe sole was required for proper fitting of the nylon insole into the shoe (Figure 3.13).

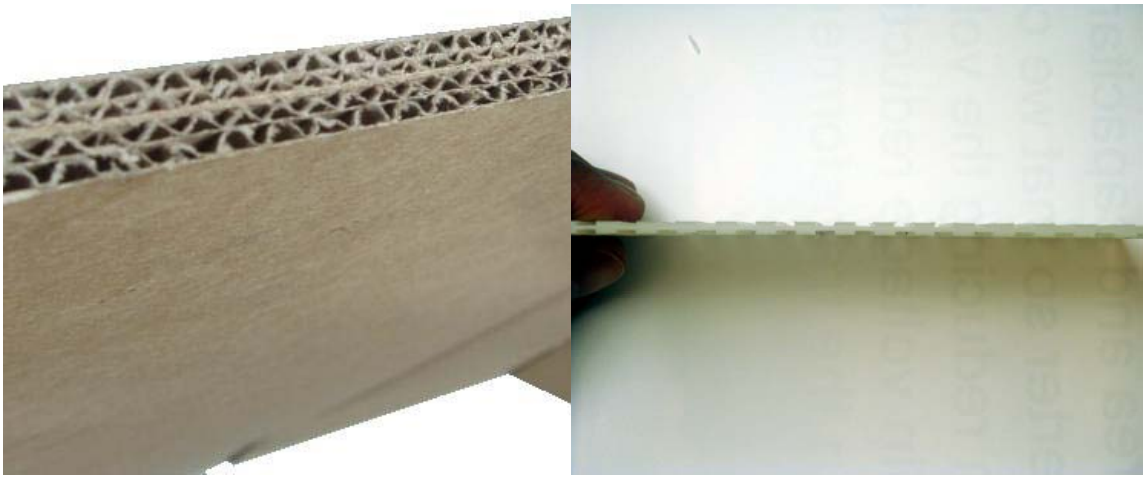

Figure 4.11: Etched Nylon Insole Core and Inspirational Cardboard Construction

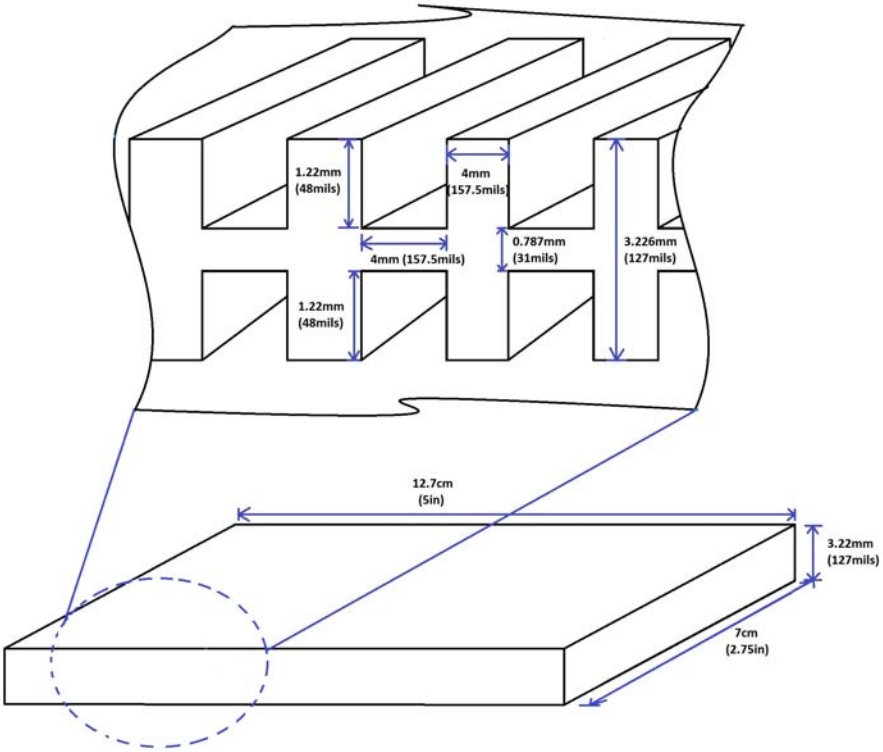


Figure 4.12: Double Side Etched Nylon Insole Core Dimensions

Once the insole has been etched, the depressions need to be filled in order to provide an even surface for the proper adherence of the PVDF sheet to the insole. Although various filling materials were investigated, insulation caulks were found to be the optimal materials because of their application mechanism, the pump, allowed for easy filling of the depressions. DAP-45390, a flexible clear synthetic rubber based caulk was chosen because, unlike silicon based caulk, it is not adhesive resistant and it adheres to nylon better than either acrylic or polyurethane based caulk.

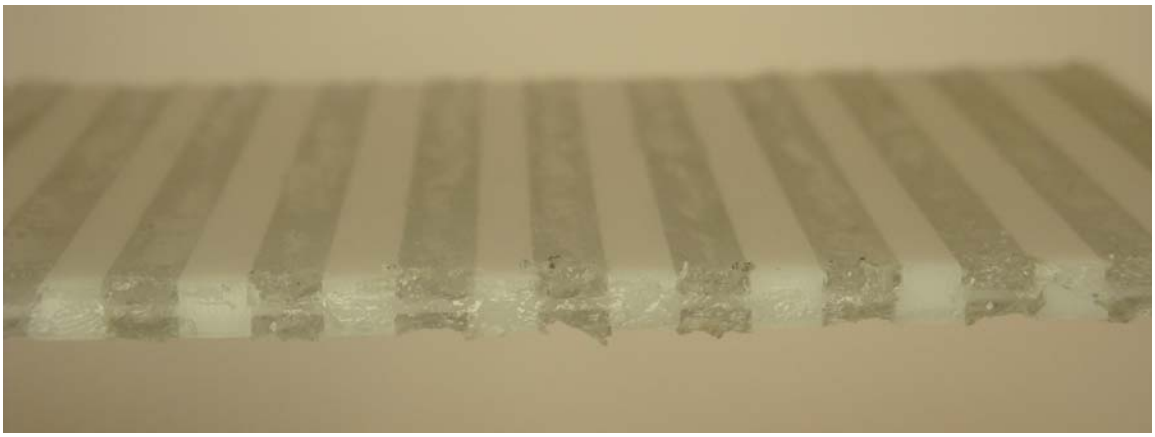

Figure 4.13: Double Side Etched Nylon Insole Core Filled by Synthetic Rubber Caulk

After initial tests two significant problems arose: the compression side exhibited significant "bulging/blubbing" and electrodes on the tension side often disconnected. The "bulging/blubbing" of the compression side has occurred in all previous insole designs; the extreme force at the compression point lifts and separates PVDF sheets from the insole core. However, now, the material density difference between the nylon insole and the synthetic rubber caulk caused significantly more uneven "bulging/blubbing" on the first PVDF layer which transcends to the layers adhered on top. (See Figure 4.14) This increase in "bulging/blubbing" decreases the power output of the compression side by over 25 times for each PVDF layer. In order to avoid this, only the tension side of the insole core was etched as opposed to etching both tension and compression sides. This leaves the compression side flat, eliminating the bulging/bubbling but resulted in power output loss. The second problem that arose involved electrodes on the tension side disconnecting. The etched out space that enabled the flexibility in turn created gaps,

stretches, and tears in the electrodes resulting in breakage. (See Figure 4.15) These separations result in unusable insole pieces. In order to fix these disconnections, the PVDF sheets must be peeled back and the electrode reapplied; however, the high peel strength of DP-105 epoxy caused any attempt of peeling to destroy the PVDF as well. A final improvement made to the insole core alleviated this problem by etching out the insole core to accommodate the electrode prevented any further disconnections without having to sacrifice either flexibility or thickness. (See Figure 4.16 and 4.17 for final design and resulting insole)

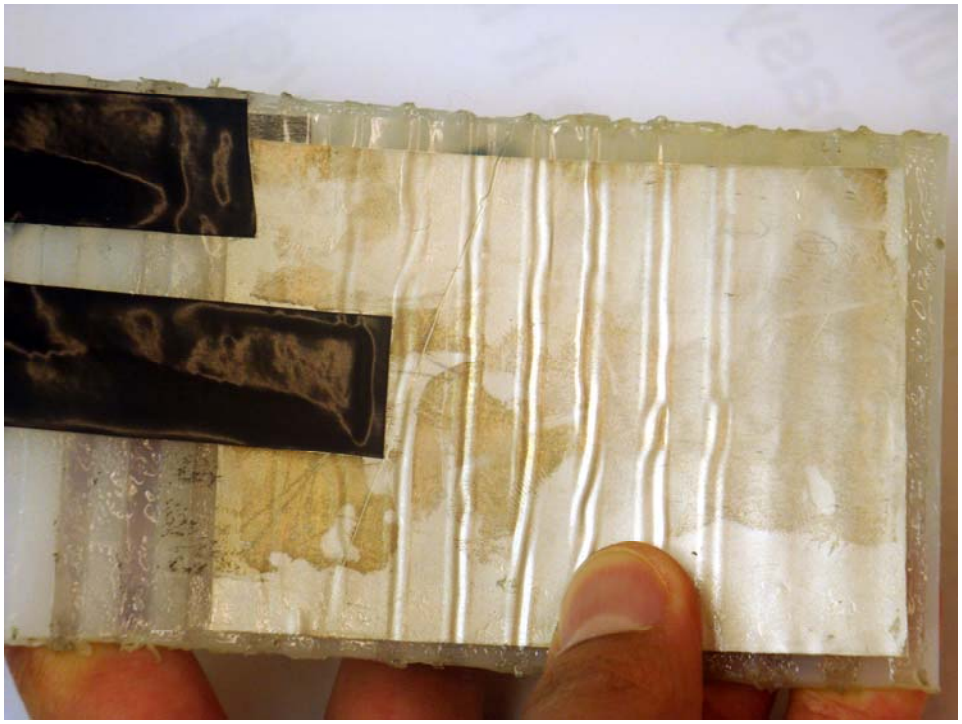

Figure 4.14: Significant "Bulging/Bubbling" of PVDF Sheet Caused by Etched Insole Core

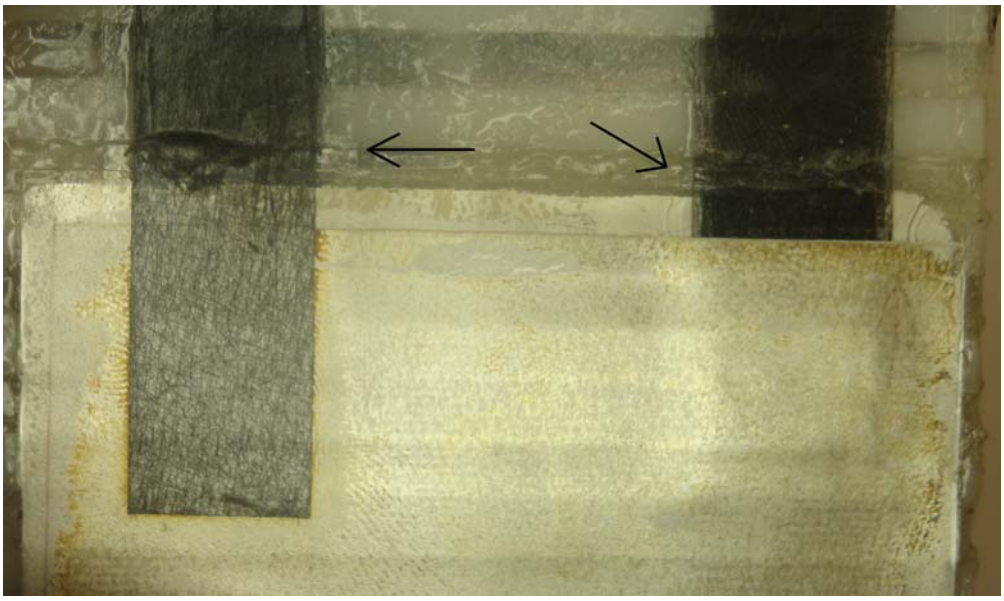

Figure 4.15: Electrodes Disconnect Caused by Bending of Etched Insole Core

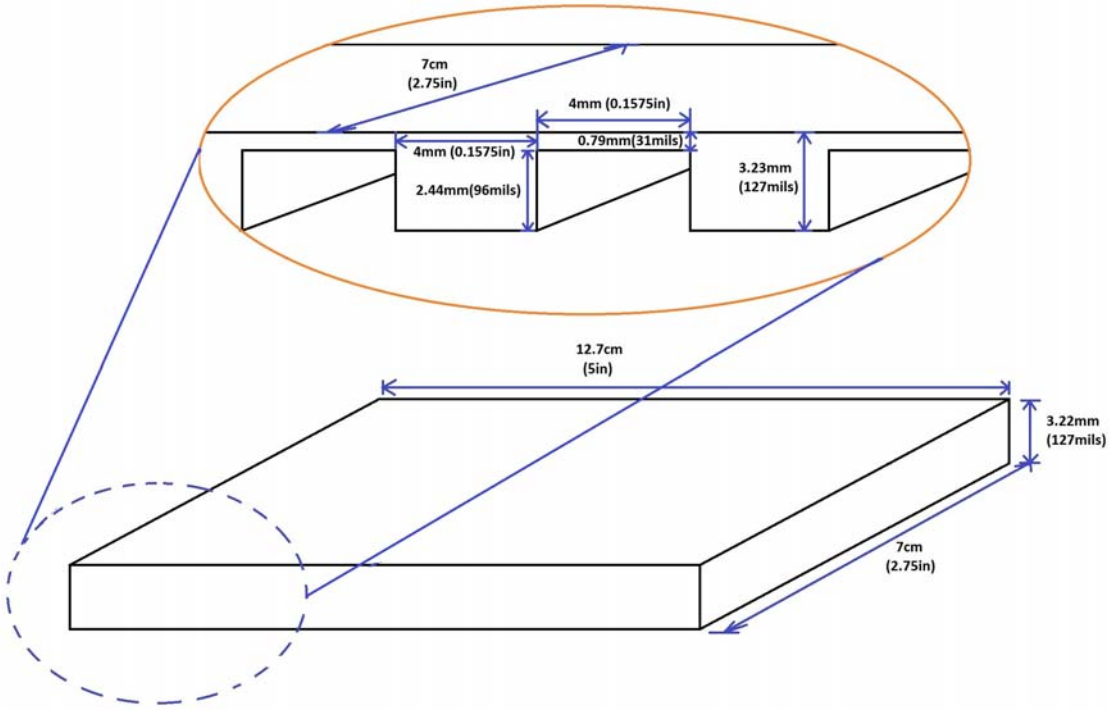


Figure 4.16: Final Propulsive Phase PVDF Insole Core Dimensions

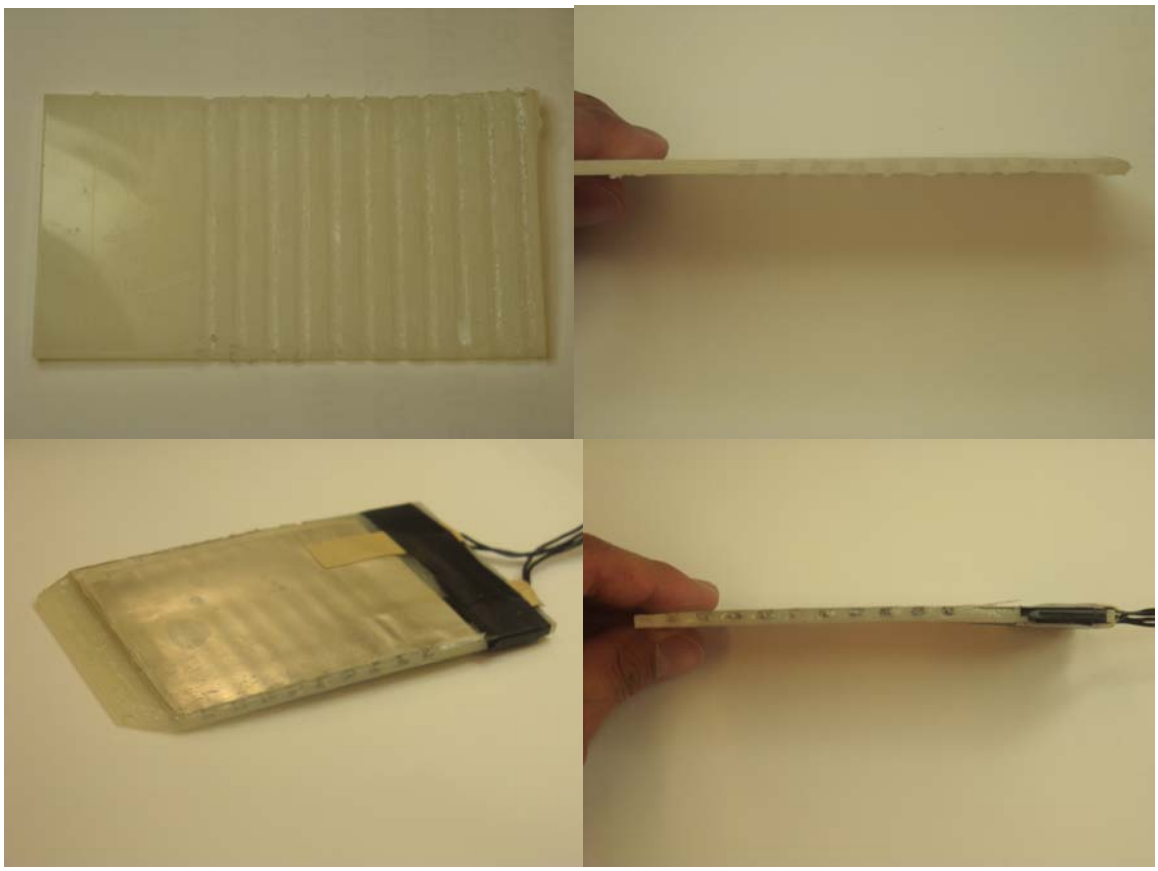

Figure 4.17: Final Propulsive Phase PVDF Insole Core. (Top Left) Surface of final insole for tension PVDF sheets, note the etched and none etched portions of insole to prevent electrode disconnect. (Top Right) side profile of final insole, note that only one side of insole is etched. (Bottom Left) Completed insole with PVDF sheet adhered to both sides and electrodes connected. (Bottom Right) Side profile of completed insole with electrodes attached.

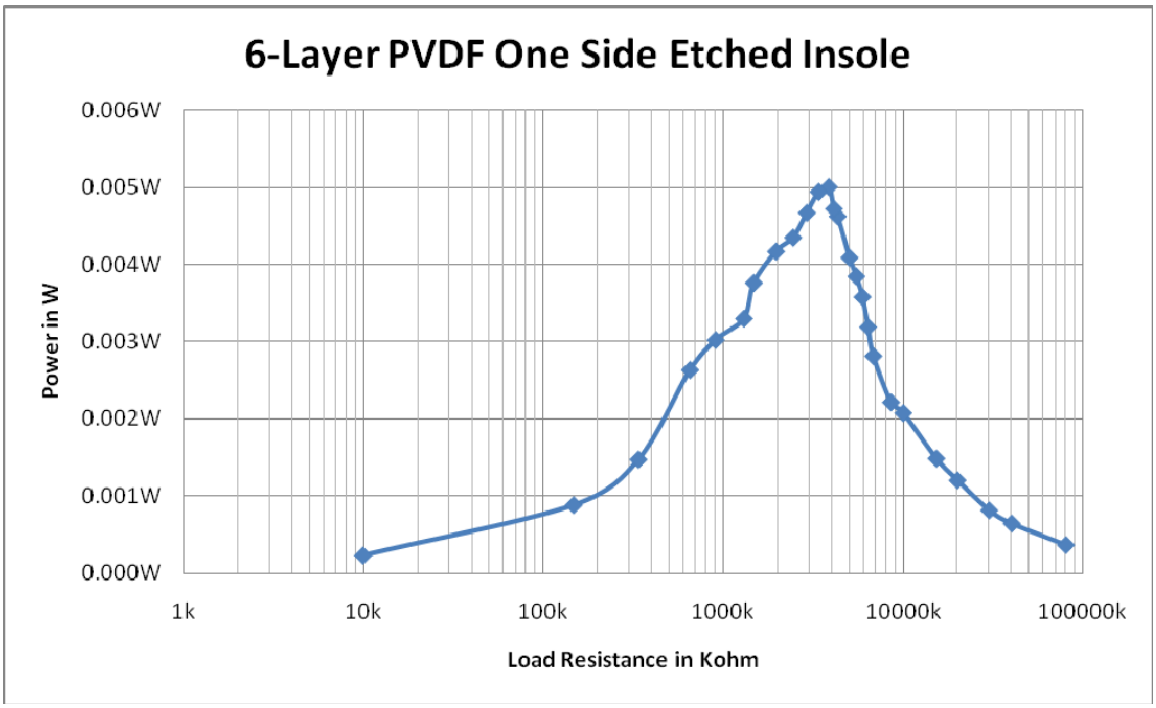


Figure 4.18: Final PVDF Insole Core Power Curve, with maximum at 4.167MΩ and 4.93mW.

Even with this new insole core flexibility, each additional PVDF layer the substrate compounds the insole's rigidity. Once three layers of PVDF were adhered to both sides the insole core reached a level of stiffness that was still comfortable for users however any further layer increase would cause interference to users' movement. With six PVDF layers, Equation 4.3 calculates optimal load resistance to 4.167MΩ, the maximum power extracted at the optimal load was measured at 4.93mW (See Figure 4.18 for Power Curve). This new design achieved the same power output, with six layers, as the eight layer insole did from previous design.

# CHAPTER 5

**Contact Phase PZT Design**

This chapter documents the design process for the "Contact Phase" piezoelectric harvester. The goal is to develop a comfortable and durable insert that would fit within a 17mm high sole as shown in Figure 3.13. First, two piezoelectric materials were considered for use in energy harvesting: PZT ceramic stacks and Thunder PZT actuators. Various designs were tested for both materials; however, Thunder PZT actuators were ultimately selected for the "Contact Phase". Second, the unimorph reverse clamshell design was finalized for use with the Thunder PZT actuators. Maximum power measurements were taken for the conventional full-wave rectifier.

## 5.1 PZT Stack

PZT ceramic stacks were first considered since their compact size and high energy density proved very attractive for the "Contact Phase" energy harvesting. The stacks' mode of operation and height are the major constraints for under the heel operation. Comparison between Table 2.4 and Figure 3.13 clearly shows that while the height of PZT stack is 18mm, the shoe sole height is already 17mm. This poses a potential problem for usability. If the PZT stacks were stood up there would be no shock absorbing materials between the heel of the foot and the PZT/ground, which could be

very uncomfortable for the user. Therefore, the PZT stack must be place horizontally to avoid user discomfort. Thus the challenge is to convert the downward force of the "Contact Phase" into xy-plane compression. The first apparatus designed to convert the downward "Contact Phase" force was inspired by clamps. (See Figure 5.1)

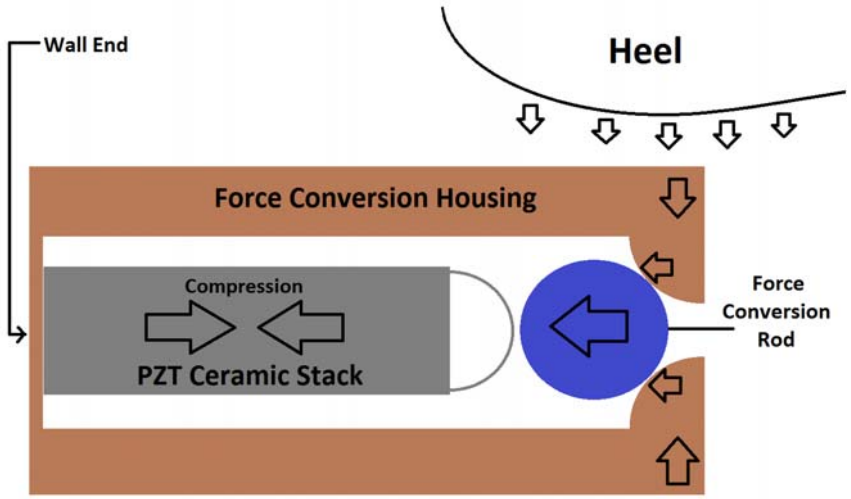


Figure 5.1: PZT Stack Construction and Force Diagram

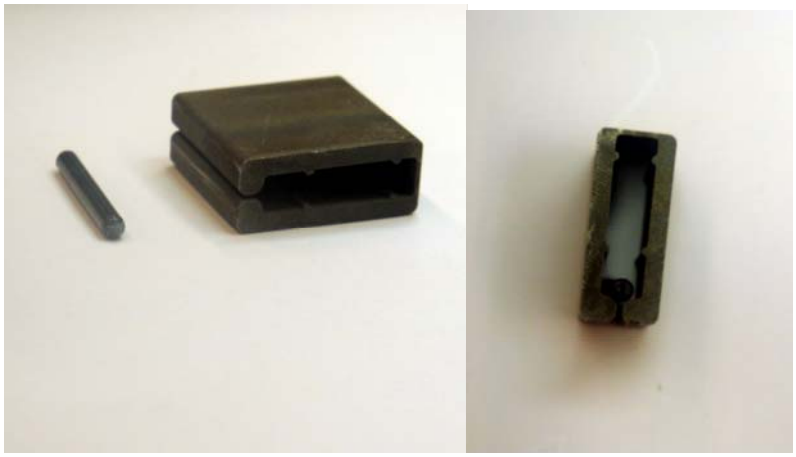

Figure 5.2: First PZT Stack Housing Design

The resulting PZT stack housing inspired by the clamp, which can be seen in Figure 5.2, did not perform well. Little to no downward force was transferred into horizontal compression during normal walking. The oscilloscope only registered voltage potential across the stacks when pliers were utilized to force the clamps down. The main factor contributing to the non-transference of downward force into xy compression is believed to be the rigidity of the housing clamp's "wall end". Despite downward force bending the clamp at one end, by remaining rigid wall end prohibited the proper compression of the housing clamp as a whole. A second force conversion housing was designed to address this dilemma. (See Figure 5.3 and 5.4)

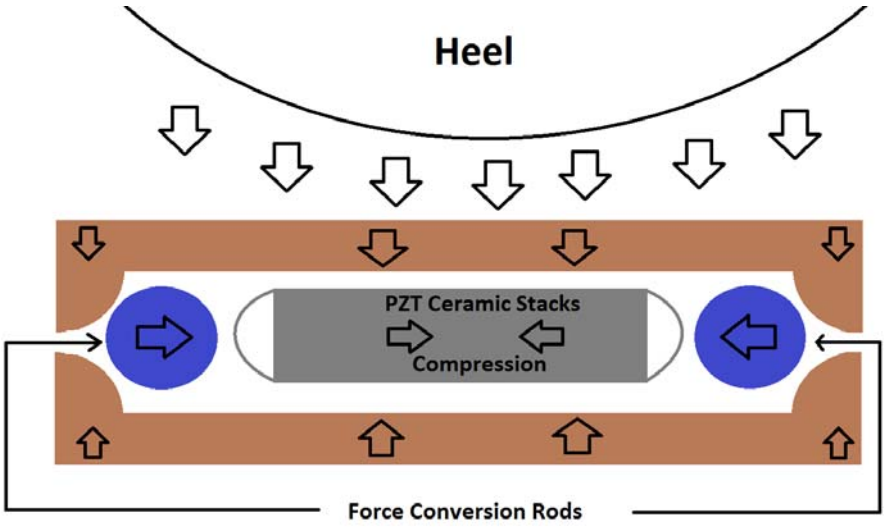


Figure 5.3: PZT Stack Construction Two, and Force Diagram

Figure 5.4: Second PZT Stack Force Transfer Design

The new PZT Stack construction alleviated the previous design dilemma of the wall end's inflexibility prohibiting proper force conversion, by allowing compression of the whole housing surface. This improvement drastically improved the power output; however after only a few trial experiments it became apparent this housing unit caused considerable damage to the PZT stacks. (See Figure 5.5) On the one hand, the PZT Ceramic stacks are easily damaged by any force applied to the stacks outside of its center cross-section. On the other hand, the force conversion rods need to be free floating because they are used to transfer vertical compression to horizontal compression. Yet, with free floating force conversion rods, the horizontal compression forces can easily shift outside of the stack's center cross-section causing damage to the PZT stacks. The damages significantly reduced the piezoelectric properties of the stacks; no meaningful power output could be measured. Without any other plausible design solutions, the PZT stacks were no longer viable for "Contact Phase" energy harvesting, and focus was directed toward the Thunder PZT.

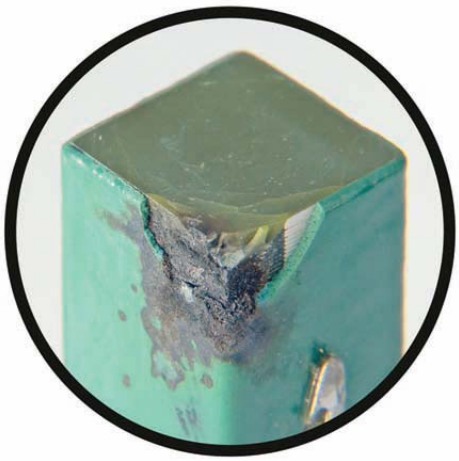

Figure 5.5: Damage caused by off-center force applied on PZT Ceramic Stacks

## 5.2 Thunder PZT Reversed Clamshell Design

Since the resting height of the TH-6R Thunder is already very small (4.24mm) and the compressed height is even smaller (Thickness of TH-6R: 0.71mm), a bimorph construction was envisioned at the onset. In order to acquire higher energy density and lower source impedance two TH-6Rs were combined together, with the total resting thicknesses coming only to 8.48mm; well under the total shoe sole thickness of 17mm. This still leaves plenty of room for shock absorbing materials and PZT protective housing. Furthermore, just like the PVDF construction, by connecting the two Thunders in parallel the available energy was doubled and the source impedance characteristics were improved, halving the optimal load resistance. Unlike the PZT stacks, Thunder Bimorph provides a much greater degree of displacement through which the heel could decelerate during the “Contact Phase”.

The PZT Thunder bimorphs were placed between two steel plates to protect them from the general demanding environment of the shoes during walking. Then four screws and screw guards were placed between the four pre-manufactured slots at the two ends of TH-6R as seen in Figure 2.3. The four screw guards limits movement to only vertical directions and prevented the bimorphs from slipping out. The Thunder pieces were placed in reverse clamshell mode so that the maximum compression occurs when the Thunder was flat. If placed in regular clamshell mode, the Thunder pieces would experience greater than necessary depression resulting in it bending in the opposite direction. This would then damage the spring steel by destroying the pre-manufactured stress curve, described in Chapter 2, rendering the Thunder pieces useless. Finally electrodes were soldered on for power extraction. The final height of this constitution is only 10mm, which still leaves plenty of space for shock absorbing sole materials to ensure user comfort. (See Figure 5.6 and 5.7)

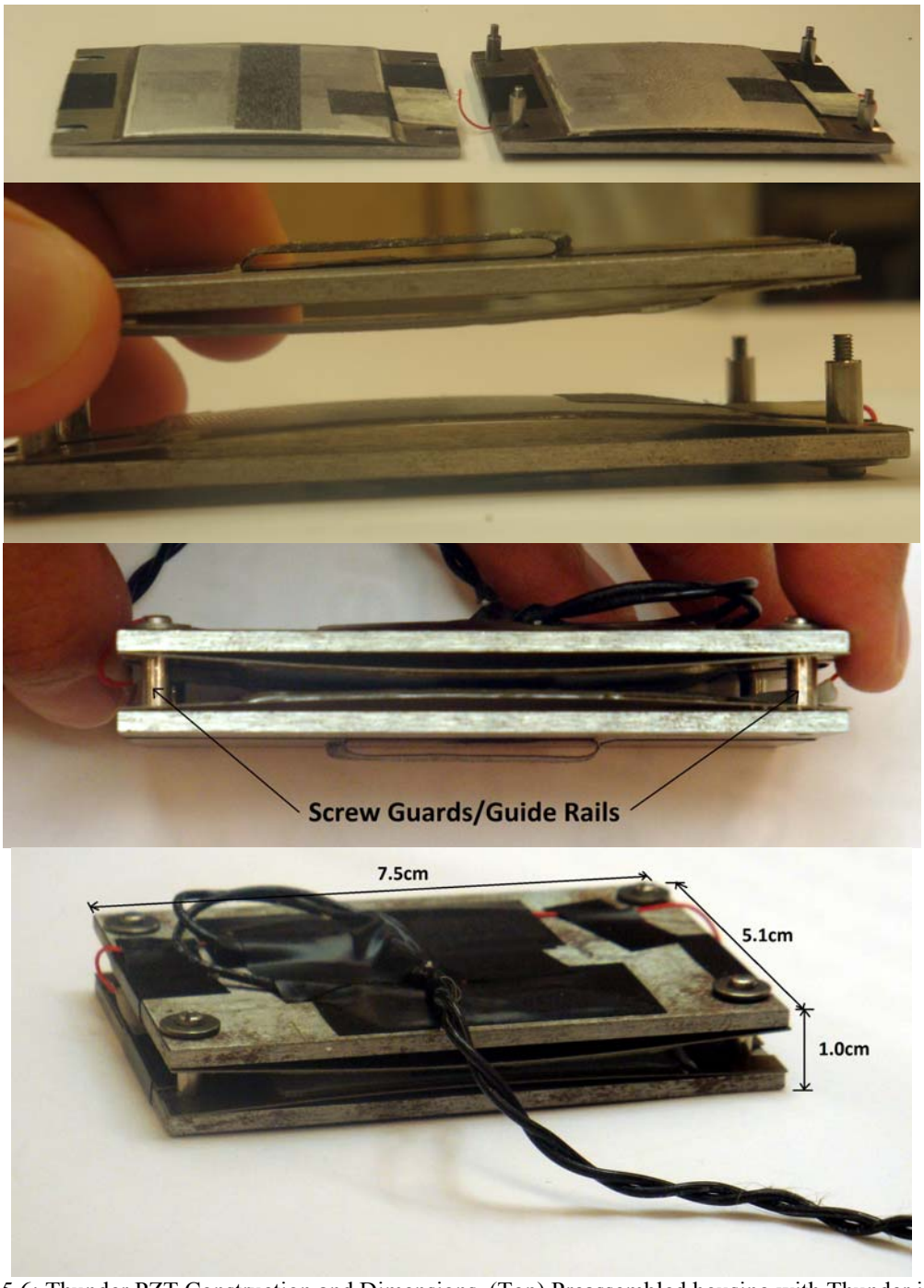


Figure 5.6: Thunder PZT Construction and Dimensions, (Top) Preassembled housing with Thunder in place and electrodes connected. (2nd TOP) Thunder side profile with housing nearly connected. (2nd Bottom) Side profile of Thunder PZT insert with Screw Guard/Guide Rails Displayed. (Bottom) Completed insert with dimensions

Since the power extraction circuit is identical to the PVDF (Figure 2.3) along with the same optimal resistance equation (Equation 2.3), the same full wave power extraction circuit is used (Figure 2.4). Power measurements were obtained by placing the insole under the shoes and walking while connected to a full wave rectifier and multimeter. (See Figure 4.3) For the bimorph Thunder insert, the source capacitance was 150nF, via Equation 2.4 the optimal load resistance was at 1.66MΩ. As done previously, a set of other load resistances were used for measurements to capture the power curve. (See Figure 5.8) With an optimal load resistance of 1.48MΩ, maximum power extracted with the full wave rectifier was 5.94mW. The optimal load resistance difference, from the one calculated from Equation 2.3, may be due to a faster walking speed during testing, which could not be precisely calibrated to one step per second.

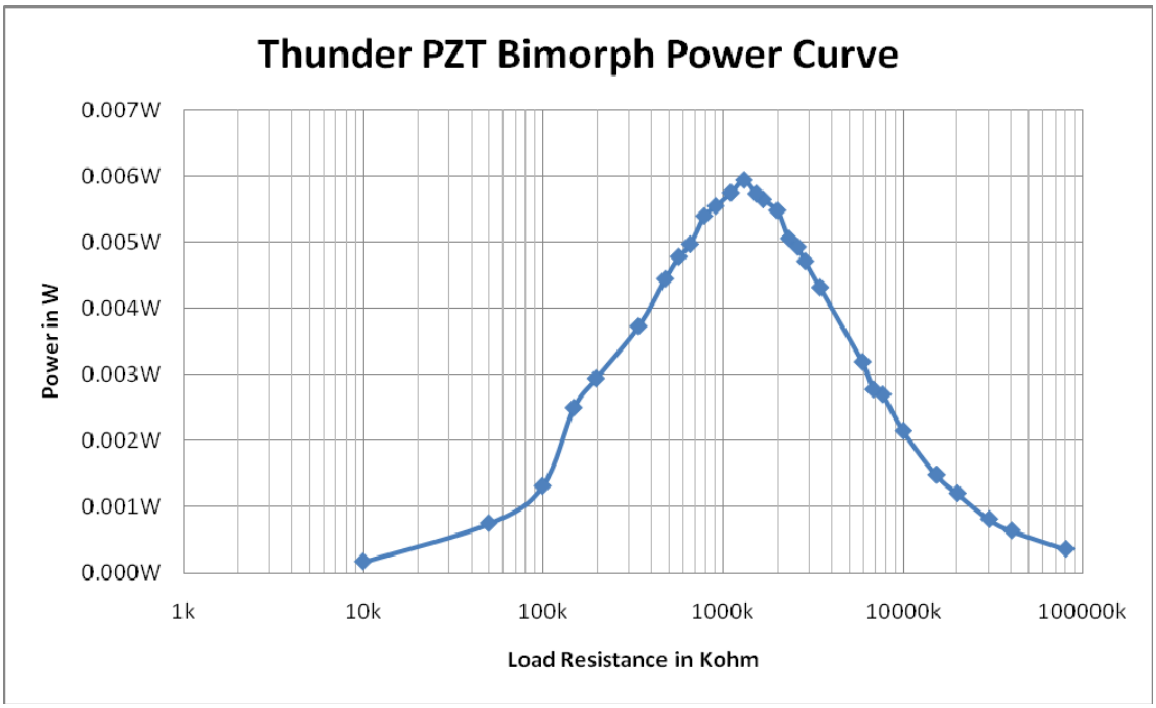


Figure 5.8: Thunder PZT Bimorph Insert Power Curve, with maximum power at 5.94mW over 1.48MΩ load.

# CHAPTER 6

## Power Extraction Circuit

Piezoelectric power sources, like the one investigated in this project operating at extreme low frequencies (~1Hz), requires resonant systems for proper power extraction. However, with such low frequency, direct electrical resonance with large inductor is impossible. Thus in previous studies by Robbins/Morris [7], quasi-resonant circuits are used to overcome this limitation by a synchronized switch system over a series inductor between the load and source. The Synchronized Switch Harvesting on Inductor (SSHI)

circuit have been successfully used for energy harvesting of wind power PVDF flags, which increased maximum power output by a factor of 3.5 over standard full wave rectifier method [7]. This chapter will go over the quasi-resonant SSHI circuit design, along with the boot-strap micro-power regulated step-down converter that is used to power the SSHI from the piezoelectric source. Then various improvements in design and necessary customization of the circuit for self powered Piezo elements are detailed. The results from using the circuit for power extraction and analysis are then presented in the following Chapter 7.

## 6.1 SSHI Circuit Overview

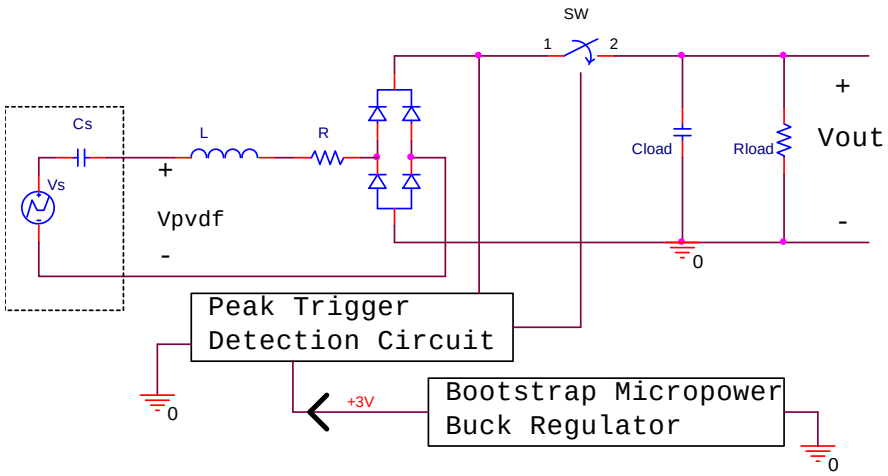


Figure 6.1: SSHI Circuit Diagram showing peak detection circuit, transistor switch, and bootstrap startup/micro-power buck regulator.

The SSHI circuit consists of an inductor connected in series to the piezoelectric source, a bridge diode rectifier, peak detecting circuit, and finally a BiMOS switch. Figure 6.1 details the SSHI circuit diagram, showing the inductor placed on the

piezoelectric source side of the full wave bridge rectifier. This is done due to experimental results from previous Robbins/Morris study, which found this placement to be 23.5% higher power output than placing the inductor on the load side of rectifier. The inductor is followed by a resistor to schematically/PSpice represent the real resistance of none ideal inductor L, due to the resistivity of wires and losses in core material. When the inductor is resonating with the capacitance of piezoelectric material, this resistance is one of the main factors for loss and low Q rating which would degrade the circuit performance. The inductor is custom made to fulfill two key requirements, low power dissipation (low R) and very high inductance. With no commercially available inductors satisfying those requirements, the Robbins/Morris study constructed their own inductor. A custom made, 0.92H inductor with series resistance of 15Ω was used in this project. The design and calculations are attached in Appendix A.

### 6.2 Peak Detection and Triggering Circuit

As shown in Figure 6.2, both Piezoelectric source signals from the PZT and PVDF elements consist of two peaks, the first from initial excitation and the second from equalization of the Piezoelectric material after excitation. . Also displayed in Figure 6.2, the two peaks of source signals are vastly different, with the first peak much higher than the second peak (2-4 times higher) and the second peak being much wider peak than the first. The initial Robbins/Morris peak detection circuit (Figure 6.3) consisted of one

voltage divider connected to positive input terminal of comparator TLV3701; while a second voltage divider and a capacitor (low pass filter) is used to achieve a DC signal for the comparator to compare with and obtain the output peak indicator. However, that design was for a sinusoidal waveform with equal ac amplitude, which is much different from the pulse like waveform presented here.

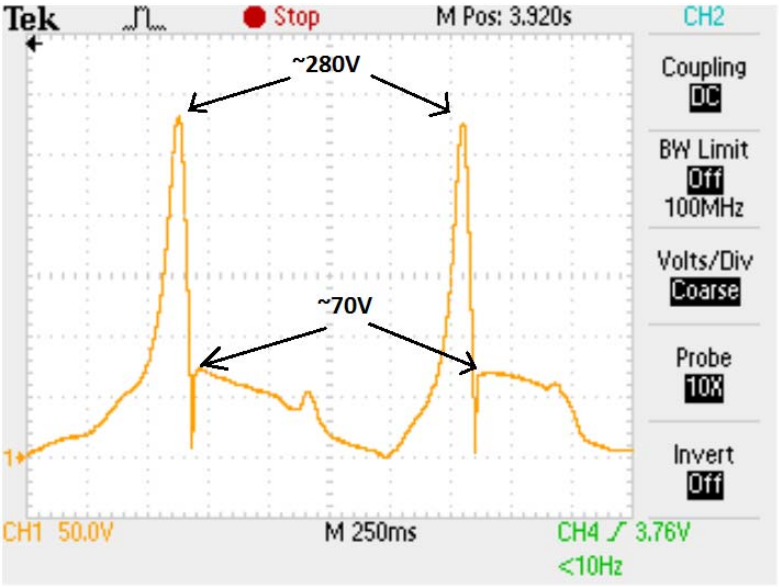

Figure 6.2: Piezoelectric Source Signal from PVDF insole

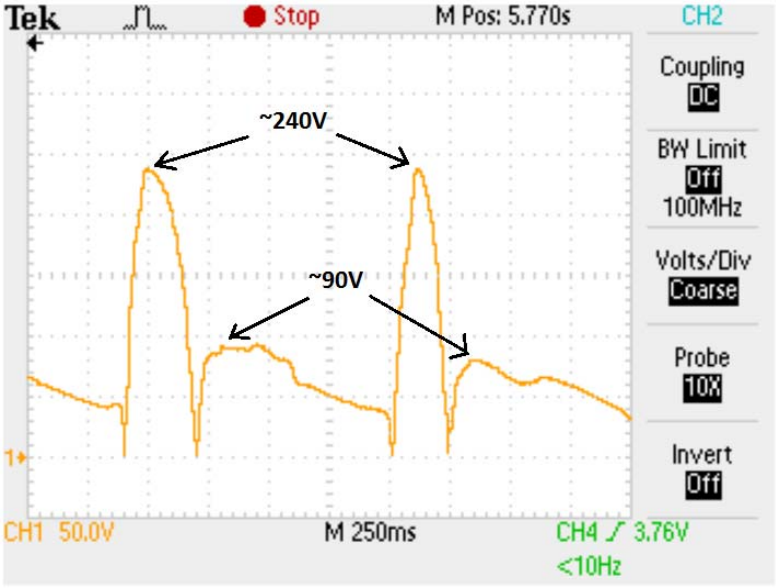


Figure 6.3: Piezoelectric Source Signal from PZT Thunder insert

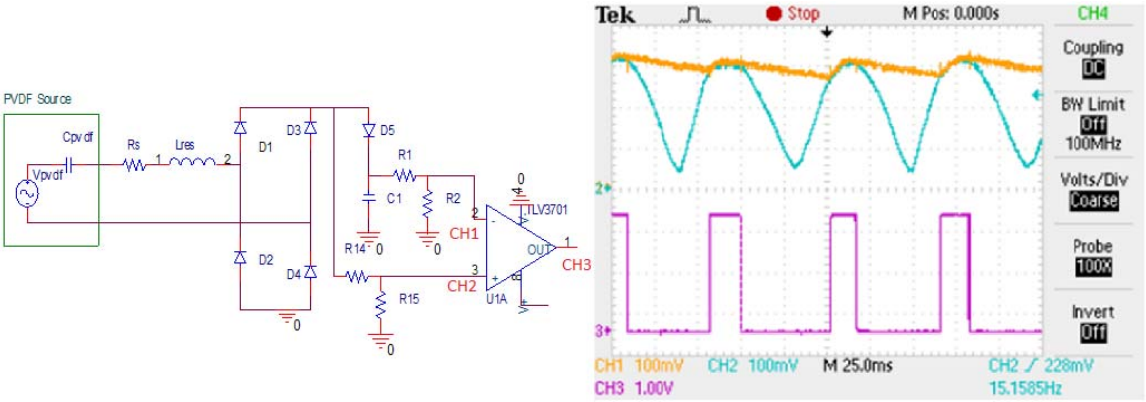


Figure 6.4: Robbins/Morris Peak Detection Circuit and Resulting Waveforms

Not only is there a difference between the amplitude of the two peaks, the frequency for which each peak appears is also dissimilar. The period length from the first to the second peak is much faster than the period length from the second to first peak (as shown in Figure 6.2). This difference in frequency forces the capacitor C1 to drain more

between the second and first peak than the first and second peak, triggering the comparator at different areas of each peak which results synchronization switching error. No combination of capacitor and resistor in the low pass filter could capture both peaks. Therefore, it was decided that the peak detection circuit would only look for the first peak, where the most energy is present. An alternative circuit was then designed to reduce complexity and power loss: the peak detection and triggering circuit consists of full-bridge rectifier, one voltage divider, self referencing comparator, and two multi-vibrators. Figure 6.4 details the schematic.

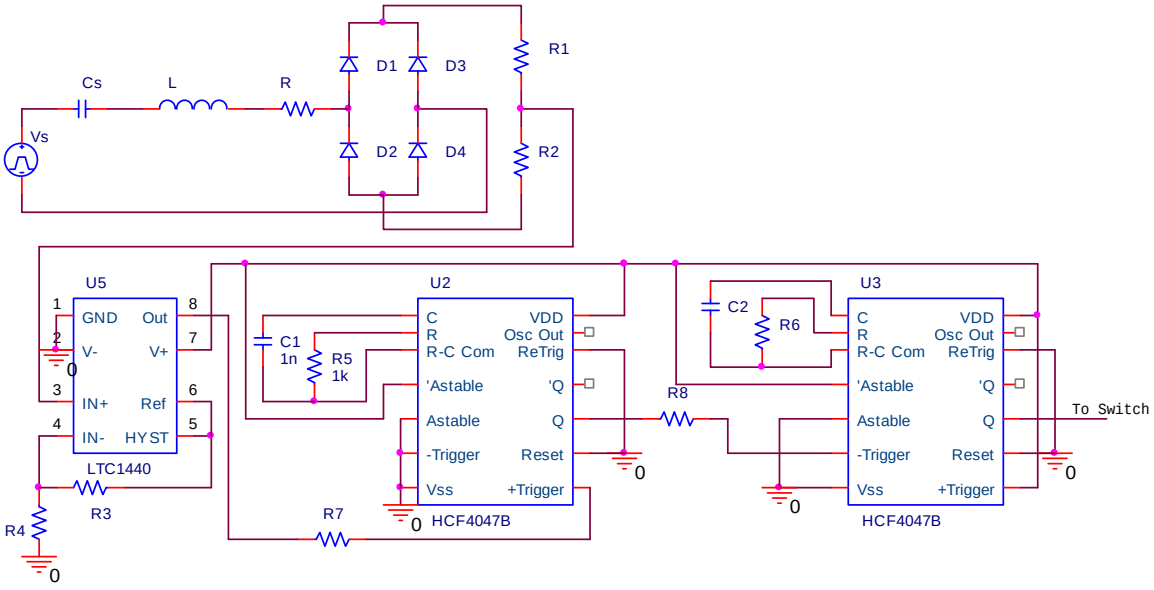


Figure 6.5: SSHI Schematic of Peak Detection and Triggering Circuit

The peak detection circuit used has one voltage divider (R1/R2: 200MΩ/1MΩ) which scales down the rectified piezoelectric signal down to less than 1.4V for PVDF (1.2V for PZT). Additionally, it is connected to the positive input terminal of LTC1440

comparator. The LTC1440 comparator has a built in reference voltage of 1.182 when operating from 2-11V. The reference voltage is also scaled down by a voltage divider (R3/R4) and connects to the negative input of comparator so the comparator goes high when the piezoelectric source is above 250V for PVDF (and 200V for PZT). This alternative circuit removes the need for the RC peak detection circuit and reduces power lost through the additional voltage divider. Similar to the original peak detection circuit, the output of LCT1440 comparator goes high ~25ms before the actual peak of the rectified piezoelectric signal from PVDF insole, while it goes high ~35ms before the actual peak of the rectified piezoelectric signal from PZT Thunder insert. (See Figure 6.5) This early triggering will be compensated by two multi-vibrators operating in one-shot mono-stable mode.

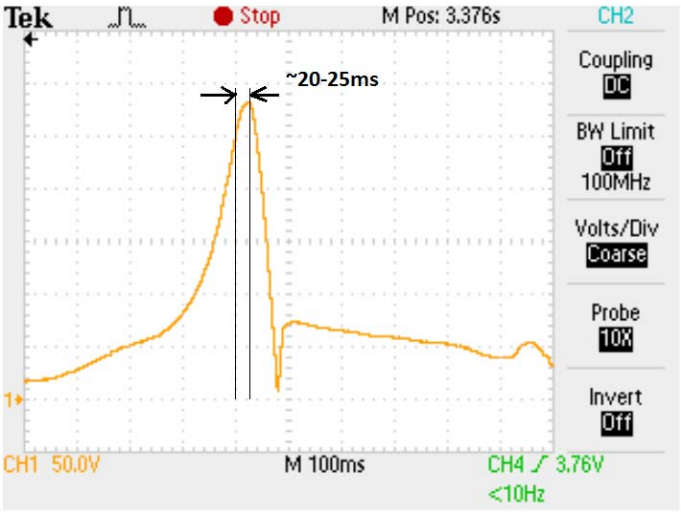


Figure 6.6: Piezoelectric Source Signal from PVDF insole showing a 20-25ms time delay between comparator trigger at 250V and the actual signal peak

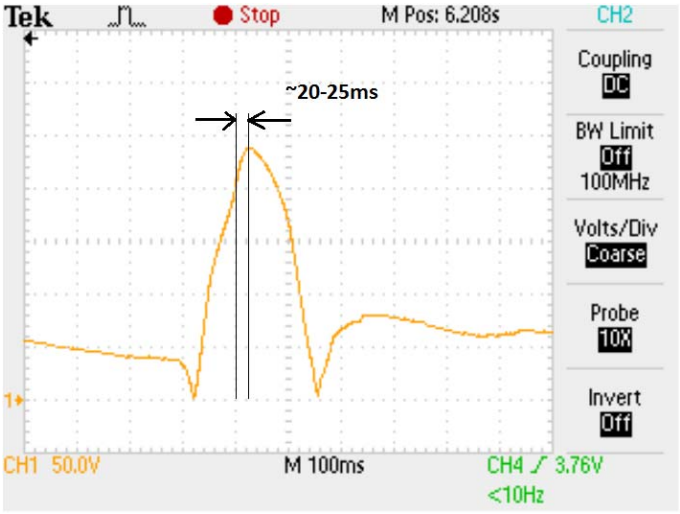

Figure 6.7: Piezoelectric Source Signal from PZT Thunder insert also showing a 20-25ms time delay between comparator trigger at 200V and the actual signal peak

In order to compensate for the early triggering of the comparator, its output is connected to a One-Shot #1 (U2) to delay the trigger for ~20-25ms, then the delayed signal is connected to One-Shot #2 (U3) for a final switch closing signal. (See Figure 6.6 for triggering circuit operational goals)

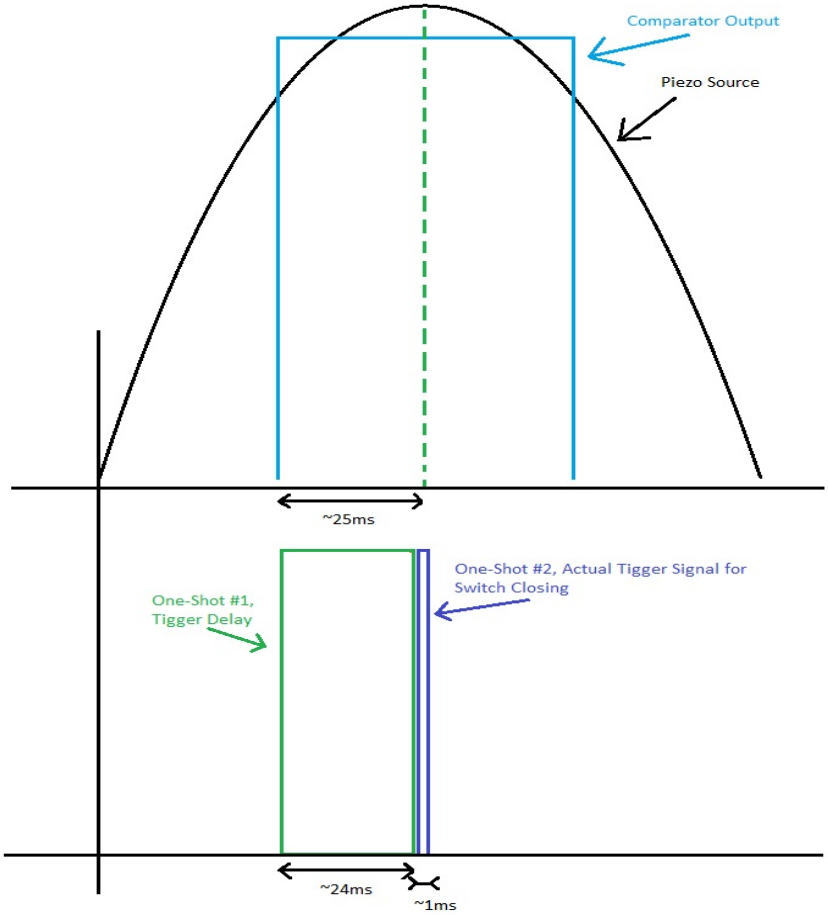

Figure 6.8: Peak Detection Circuit Waveforms of Operational Goals for PVDF Insole

The One-Shot pulse width is determined by its RC values on pin 1-3, pulse-width given by 2.48RC. The HCF4047B datasheet specifies the maximum resistance used to be 1MΩ and the minimal capacitance value to be 1nF. Following these restrictions, in order to achieve the ~24ms trigger delay in One-Shot #1 for PVDF insole, the RC values were determined to be 10nF and 0.99MΩ. The actual switch closing trigger of the One-Shot #2 must be around the half resonant period between the source piezoelectric capacitance

and the series inductance: $T = \pi * \sqrt{LC}$ . Where L is constructed at 0.92H and C is the source impedance of the PVDF insole, 60nF, the switch closed length was determined to be 0.74ms. RC values of 1nF and 400kΩ are used to achieve a pulse width of ~1ms in One-Shot #2.

### 6.3 Transistor Switch Design

The design of the switch must fulfill many requirements. The two obvious ones are a high off-state resistance and a low on-state so that the switch will behave close to the ideal. The gate was powered by the piezoelectric element, thus the transistor switch must require very little current and still achieve fast enough switching as to not degrade the resonant quality of SSHI circuit. Finally, and most importantly, the breakdown voltage can handle 350V+ from the piezoelectric sources. A NPN BJT (MPSA44) and a P-type MOSFET (FQP2P40) are used as the switch to fulfill these requirements. (See Figure 6.7 for transistor switch implementation)

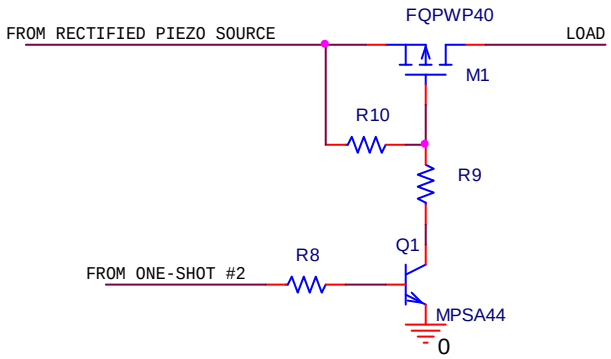


Figure 6.9: Schematic of transistor switch system for SSHI circuit

The switch close pulse signal from output of One-Shot #2 is connected to the base of BJT. When the pulse appears, current is injected into the base turning on the transistor. As the BJT is on, R9 is shorted to the ground which then allows a voltage drop across the source-gate of the MOSFET through a newly active divider network R10/R9. This voltage drop is negative across the gate-source, which turns on the P-Channel MOSFET and allows power to flow freely from a rectified piezoelectric source to the load capacitance.

Both MPSA44 and FQP2P40 have break down voltage of 400V, well above the expected maximum peak from the full-wave rectifier output of 350V. When the R10 is around 100kΩ, the PMOS switching time is on the order of 20us due to the 200pF gate capacitance, while the BJT switches much faster due to the high injecting device current (R1<R3) and the low junction capacitance of BJT.

### 6.4 Bootstrap Start-Up and Micro-Power Buck Converter

The SSHI peak detection circuit requires a stable 3V DC power source to function and maintain low power dissipation. Since the circuit is designed to operate for shoe energy harvesting, it is highly desirable that the power source comes from the Piezo element itself rather than a battery, which defeats the whole goal of this project for

remote and renewable energy harvesting. Therefore, a micro-power regulated buck converter was design and implemented.

From Chapters 4, 5 and 6, it was shown that that the PVDF insole and PZT Thunder insert have rectified voltage peaks of ~300V and ~250V respectively, and charges to 100-150V DC across an optimum load. Therefore, when the SSHI circuit operates from a cold start, the bootstrap start-up circuit must be able to accept voltages of at least 300V or more and store up enough energy for the buck convertor to function and take over the role of power source for the SSHI peak detection circuit and itself. During steady state operation, the buck converter must accept DC input up to 150V and regulate an output voltage of 3V DC. Higher supply voltage comes with higher power dissipation within those ICs, thus it is advantageous to use as low of a supply voltage as possible. The 3V supply voltage was chosen because it has the lowest acceptable operating supply voltage for the trigger circuit, which contains three ICs that operate under voltages ranging from 2.5-11V. Figure 6.8 details the schematic of the micro-power regulated buck converter with bootstrap start-up circuit.

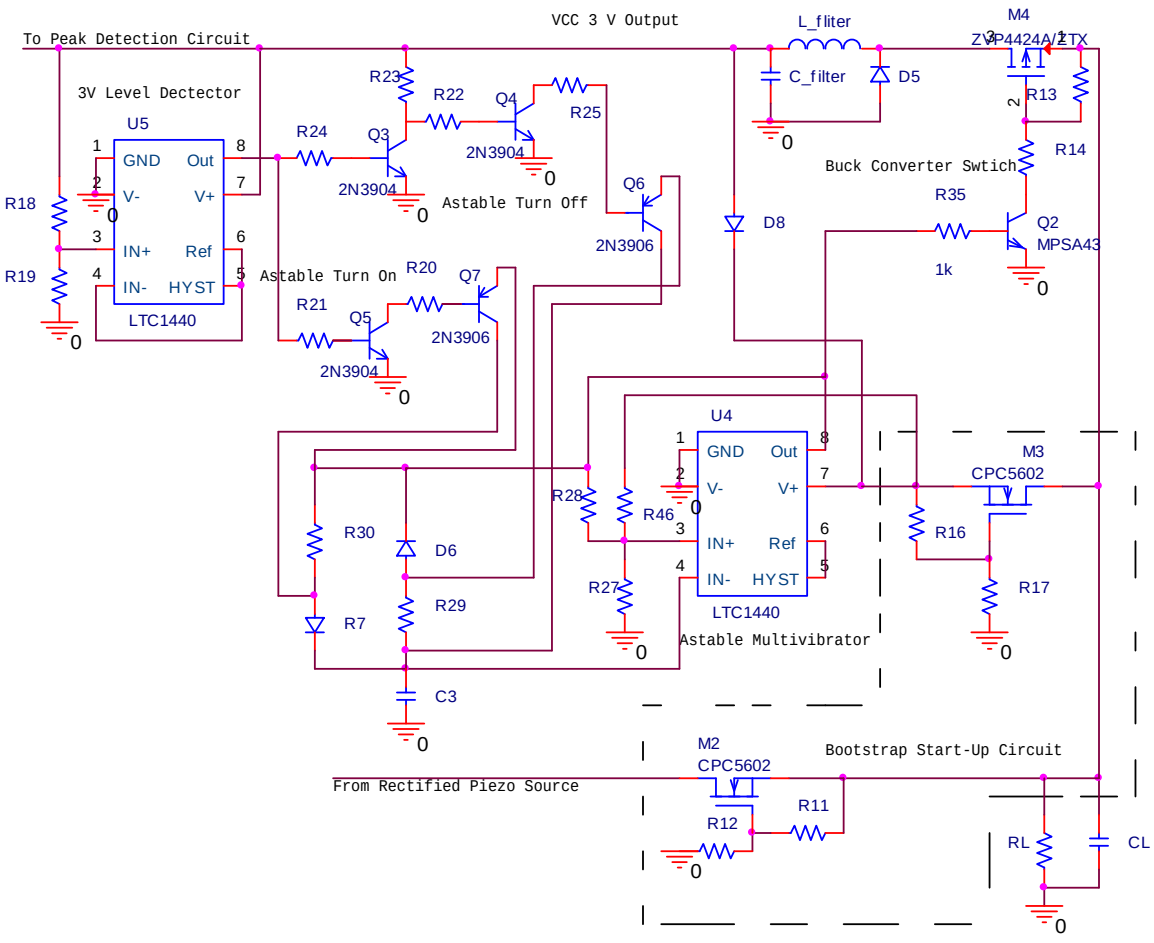


Figure 6.10: Schematic of micro-power regulated buck converter and bootstrap start-up circuit

As mentioned before, when the Piezo elements operate from a cold start, there is no 3V supply available for peak detection circuit or the buck converter. Therefore, a bootstrap circuit is used, shown in the lower right portion of Figure 6.8. The circuit utilizes Depletion mode (D-mode) MOSFET as oppose to an array of JFETs (used in Robbins/Morris study) for start-up conduction. D-mode MOSFETs come with much higher breakdown voltage variety than JFETs, eliminating the need for the JFET array

and additional expensive 200MΩ resistors. Initially the D-mode MOSFET (M2) is a short, thus allowing the load capacitance to charge up to around 4Vdc directly from the rectified Piezo element source. As soon as the load capacitance reaches 4Vdc, the voltage divider R11/R12 biases the gate-to-source voltage at negative 2 Vdc, turning the D-mode MOSFET to an open switch. For the remaining normal operation of SSHI circuit the D-mode MOSFET remains open since the load capacitance is higher than 4Vdc. A second D-mode MOSFET (M3) was used to provide 2.2V to the LTC1440 comparator (U4) to begin astable operations. The astable signal then triggers the buck converter switch (Q2 and M4) to step-down the voltage from load to the 3V Vcc filter capacitor. Once enough energy is transferred, the Vcc filtering network will have a sustained 3Vdc output, which then puts a negative 2Vdc bias across the M3 D-mode MOSFET, turning off the MOSFET. U4 will then sustain its power flow from the 3Vdc Vcc output.

Initially, the duty cycle of the astable U4 is determined by the RC integrator (C3 and R29/R30), which is approximately 1%. As the output voltage at Vcc attempts to rise higher than 3Vdc, the voltage detection comparator U5 output goes high, turning on Q5 and Q7, which shorts R30. This will decreases the duty cycle of the U4 astable, which also decrease the turn on time for the buck converter switch (M4), and thus the output voltage is reduced. On the other hand, as the output voltage falls below 3Vdc due to

lower M4 turn on time, U5 output will go low, turning off Q3 and on Q4 and Q6, which shorts R29. This increases the duty cycle of U4 astable, thus increasing the on time of M4 switch and ultimately increasing the output voltage.

A schematic of the complete SSHI circuit detailed in the following Figure 6.10, and a table with all component values is given in Table 6.1, and finally the proto-boarded SSHI circuit is shown on Figure 6.9. The trigger circuit was measured by a current meter, which found the current drawn during steady state operation to be ~10μA. Operating at 3Vdc, the trigger circuit is then measured to dissipate ~30μW. The buck converter also operating at 3Vdc, was measured by a current meter as well, and found to dissipate ~20μA or ~60μW. The over circuit then dissipates ~100μW of energy, well below the power available from the Piezo elements which were found at around 5mW using the full wave rectifier from Chapters 4 and 5.

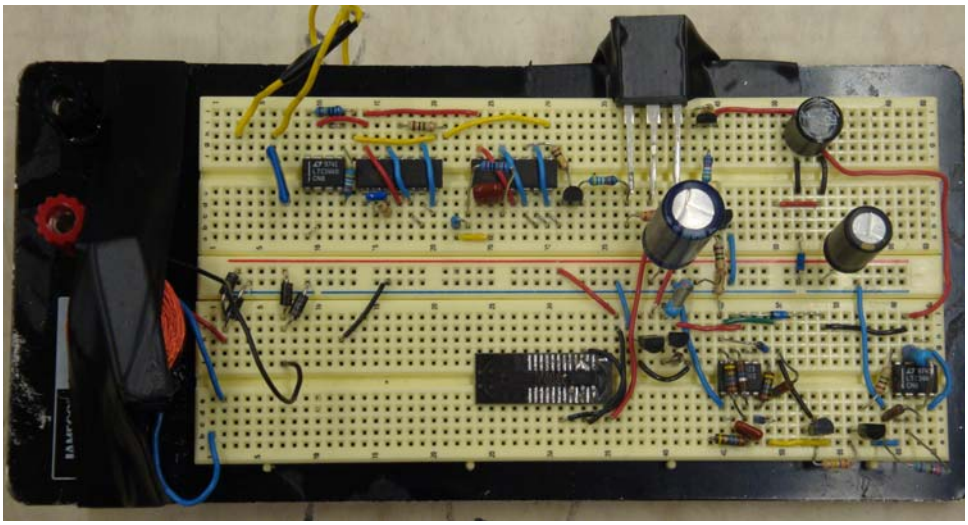

Figure 6.11: Photograph of complete SSHI circuit, including bootstrap start-up and buck converter

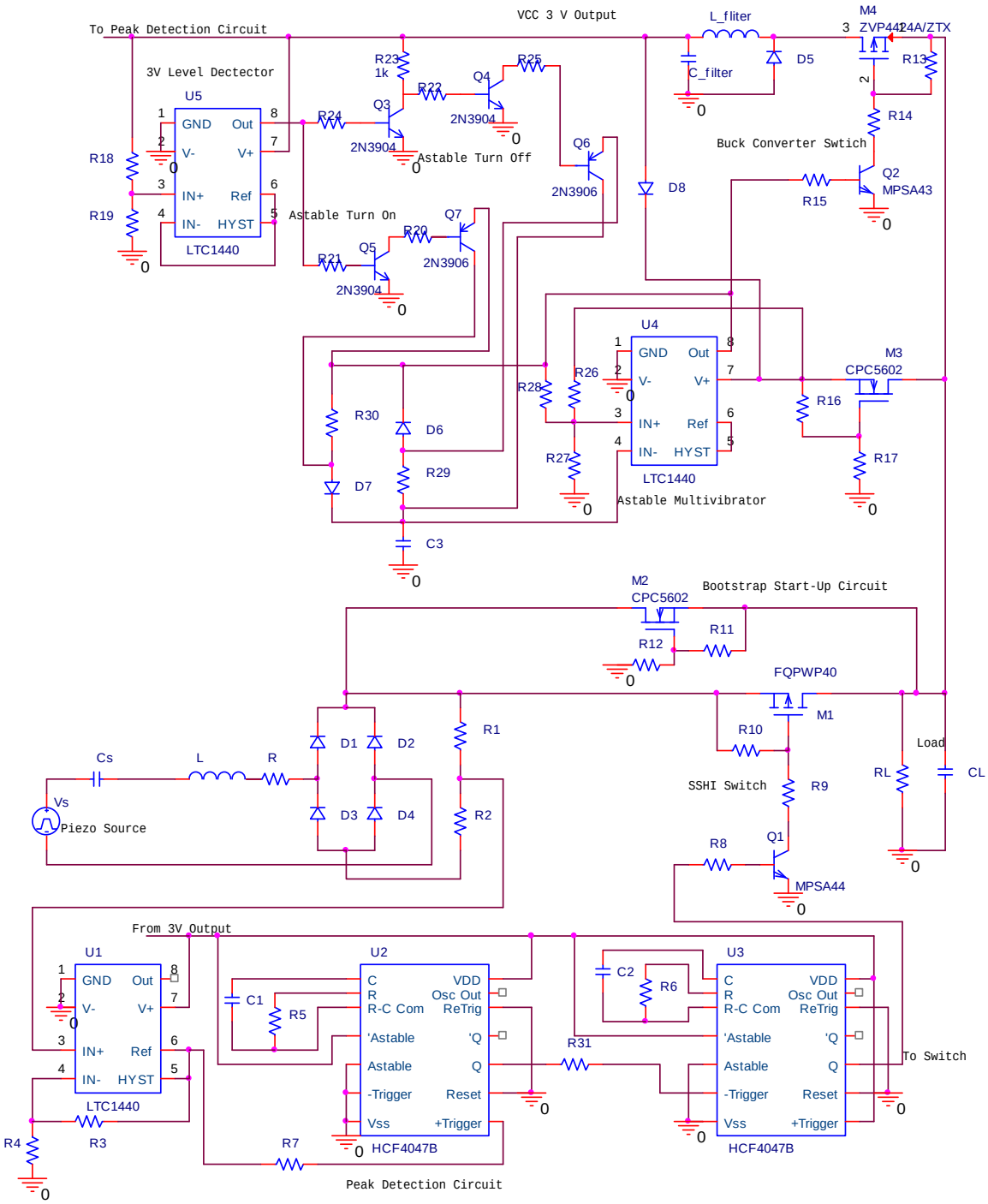


Figure 6.12: Complete Schematic of SSHI and power supply circuits

| Component | Description/Value | Component | Description/Value |
|---|---|---|---|
| D1 | HER104 – 400V | R25 | 270KΩ |
| D2 | HER104 – 400V | R26 | 20MΩ |
| D3 | HER104 – 400V | R27 | 20MΩ |
| D4 | HER104 – 400V | R28 | 20MΩ |
| D5 | BAT41 – 100V (Schottky) | R29 | 10MΩ |
| D6 | BAT41 – 100V (Schottky) | R30 | 23KΩ |
| D7 | BAT41 – 100V (Schottky) | R31 | 100KΩ |
| D8 | BAT41 – 100V (Schottky) | RL | Variable Load Resistor |
| R1 | 200MΩ | CL | 10uF |
| R2 | 1MΩ(PZT)/0.5MΩ(PVDF) | C1 | 10nF |
| R3 | 120KΩ(PZT)/685KΩ(PVDF) | C2 | 1nF |
| R4 | 500KΩ | C3 | 10nF |
| R5 | 0.99MΩ | C_filter | 1mF |
| R6 | 400KΩ | L_filter | 100mH |
| R7 | 100KΩ | M1 | FQWP40 PMOS (400V) |
| R8 | 270KΩ | M2 | CPC5602 DMOS (350V) |
| R9 | 270KΩ | M3 | CPC5602 DMOS (350V) |
| R10 | 500KΩ | M4 | ZVP4424A PMOS (200V) |
| R11 | 20MΩ | Q1 | MPSA44 N-type BJT (400V) |
| R12 | 20MΩ | Q2 | MPSA43 N-type BJT (200V) |
| R13 | 270KΩ | Q3 | 2N3904 N-type BJT (20V) |
| R14 | 500KΩ | Q4 | 2N3904 N-type BJT (20V) |
| R15 | 270KΩ | Q5 | 2N3904 N-type BJT (20V) |
| R16 | 20MΩ | Q6 | 2N3906 P-type BJT (20V) |
| R17 | 10MΩ | Q7 | 2N3906 P-type BJT (20V) |
| R18 | 20MΩ | U1 | LTC1440 Comparator |
| R19 | 12MΩ | U2 | HCF4047 Multivibrator |
| R20 | 270KΩ | U3 | HCF4047 Multivibrator |
| R21 | 1MΩ | U4 | LTC1440 Comparator |
| R23 | 500KΩ | U5 | LTC1440 Comparator |
| R24 | 1MΩ | | |

Table 6.1: Bill of Material for SSHI circuit

# CHAPTER 7

**Results and Recommendations**

This chapter reviews the work presented in this project, discusses complications encountered in implementing the SSHI system, and compares the results of each design. The best results obtained from the Piezo-elements are presented; conclusions and analysis are drawn from these results. Finally, suggestions for areas of improvements and related future work are detailed.

## 7.1 Results and Analysis

The SSHI circuit from Chapter 6 was investigated to increase power extraction. Both the PVDF insole and PZT Thunder Clamshell insert were tested with the SSHI circuit, each with a slight component value to peak detection (as listed on Table 6.1). Figure 7.1 shows the SSHI peak trigger detection circuit comparator's output vs. the actual rectified PZT insert output. The figure shows the comparator output goes high when the PZT output reaches 200V, and the triggering occurs ~25ms ahead of the actual peak, functioning as the design from Chapter 6 intended. Next, Figure 7.2 shows the rest of the peak detection triggering system. The figure details a ~23ms of time delay facilitated by One-Shot #1, followed by the actual ~1ms switch close trigger from One-Shot #2 output.

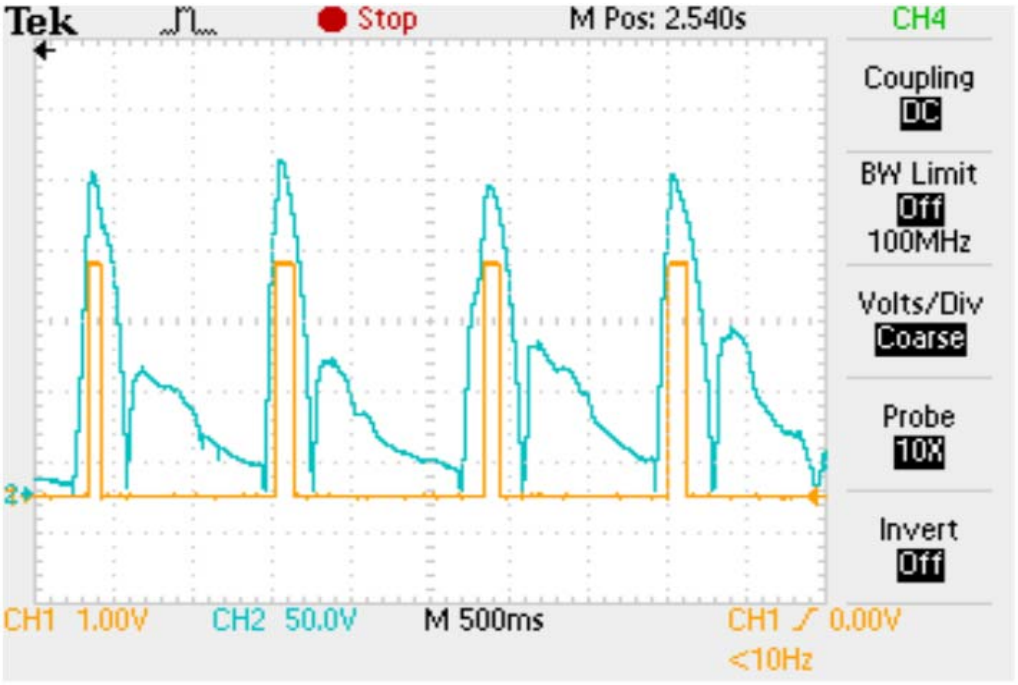


Figure 7.1: Waveforms of comparator TLC1440 output, and the PZT source output.

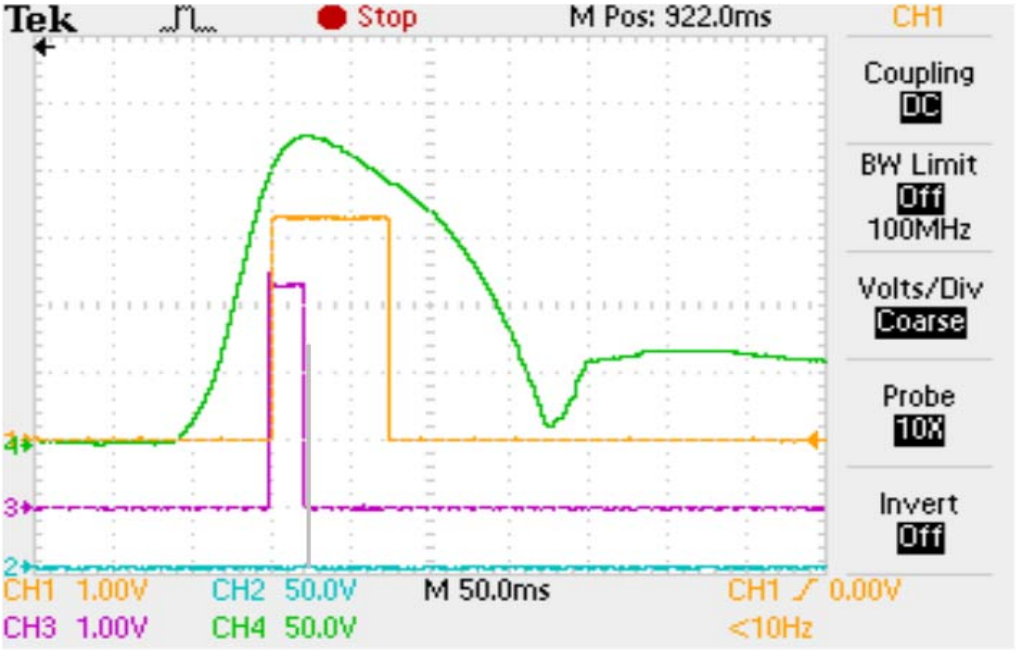


Figure 7.2: Peak detection trigger circuit waveforms of SSHI. Rectified source output (CH4, Green), Comparator output (CH1, Yellow), One-Shot #1 time delay output (CH3, Blue), One-Shot #2 switch close signal (CH2, Grey)

Once the transistor switch was implemented, the waveform behaved in an unexpected way. Figure 7.3 shows the same PZT source output from the previous figures after switching occurs. While the comparator and the rest of the trigging system was still operating as designed, the source output has been altered to produce two high voltage peaks, as oppose to the high low peaks previously observed. Figure 7.4 and 7.5 display the rectified PZT source signal along with the switch closing signals. The waveforms are near identical using PVDF insole source, and thus they are omitted.

Figure 7.3: Rectified PZT source output (CH4) along with TLC1440 comparator output (CH2) and switch close signal from One-Shot #2 (CH3)

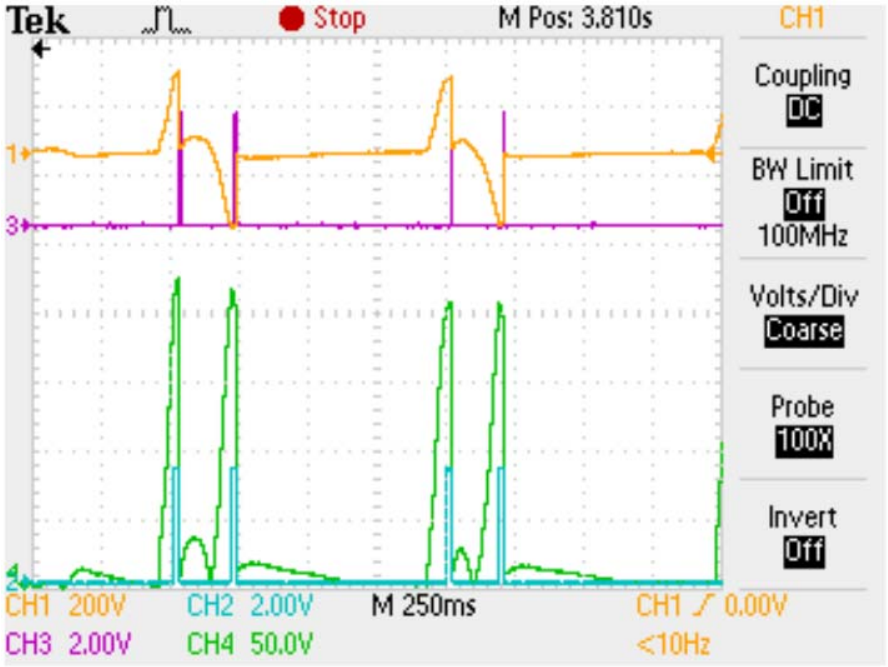


Figure 7.4: Rectified (CH4) and unrectified (CH1) source output signals, note CH1 is 200V/division, with comparator output (CH2) and switch close signal (CH3)

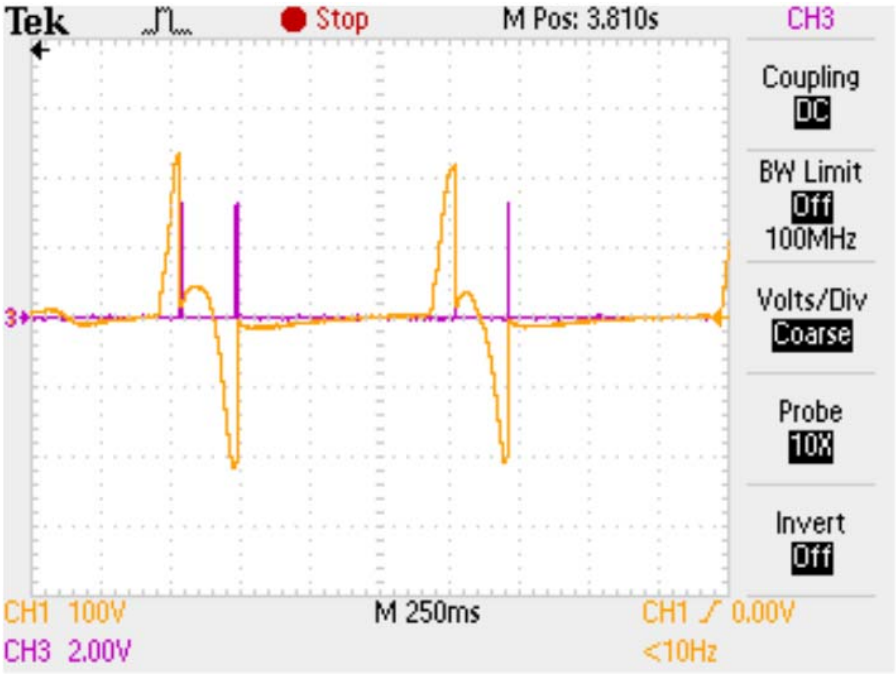


Figure 7.5: Unrectified (CH1) piezoelectric source output signals with switch close signal (CH3)

After some PSpice simulations, it was clear that by implementing the switch system the source capacitance was forced to act as a coupler capacitance. (See Figure 7.6 and 7.7) Due to the fast speed of transistor switch and immediate draining of the source to the load capacitance, the output passing through the source capacitance ceased being recognized as a dc signal and became an ac signal. The source capacitance then relays the source into an equal amplitude ac signal. The comparator then catches the second peak after rectification, which is now about the same amplitude as the first peak, and allows the trigger circuit to close the switch for the second time.

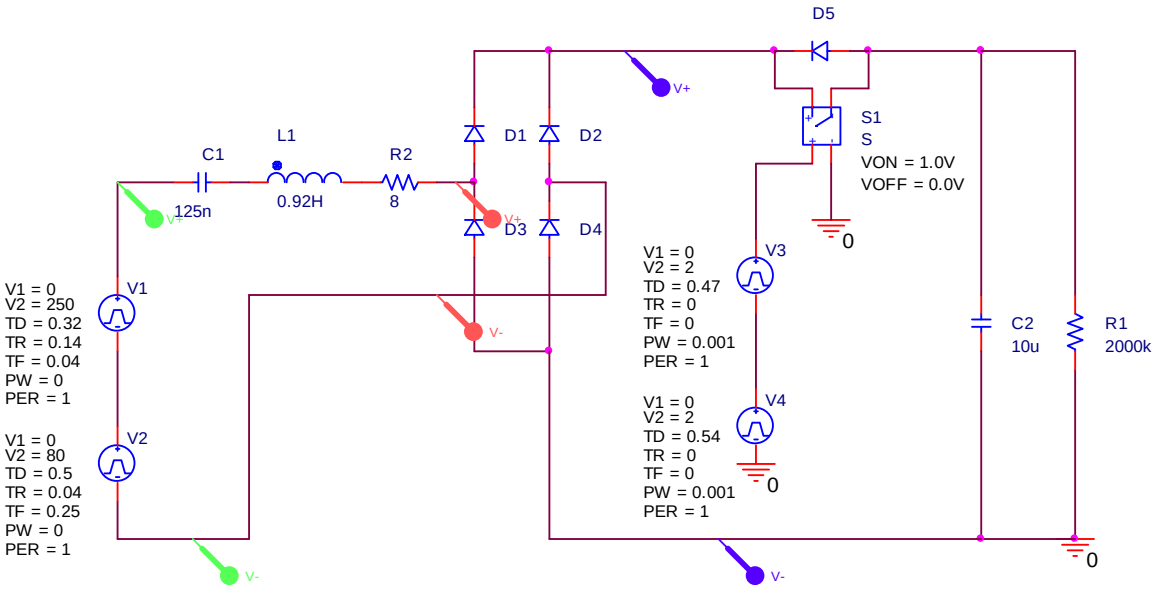


Figure 7.6: Circuit diagram for simplified PSpice simulation of trigger system to investigation piezo source signal modification.

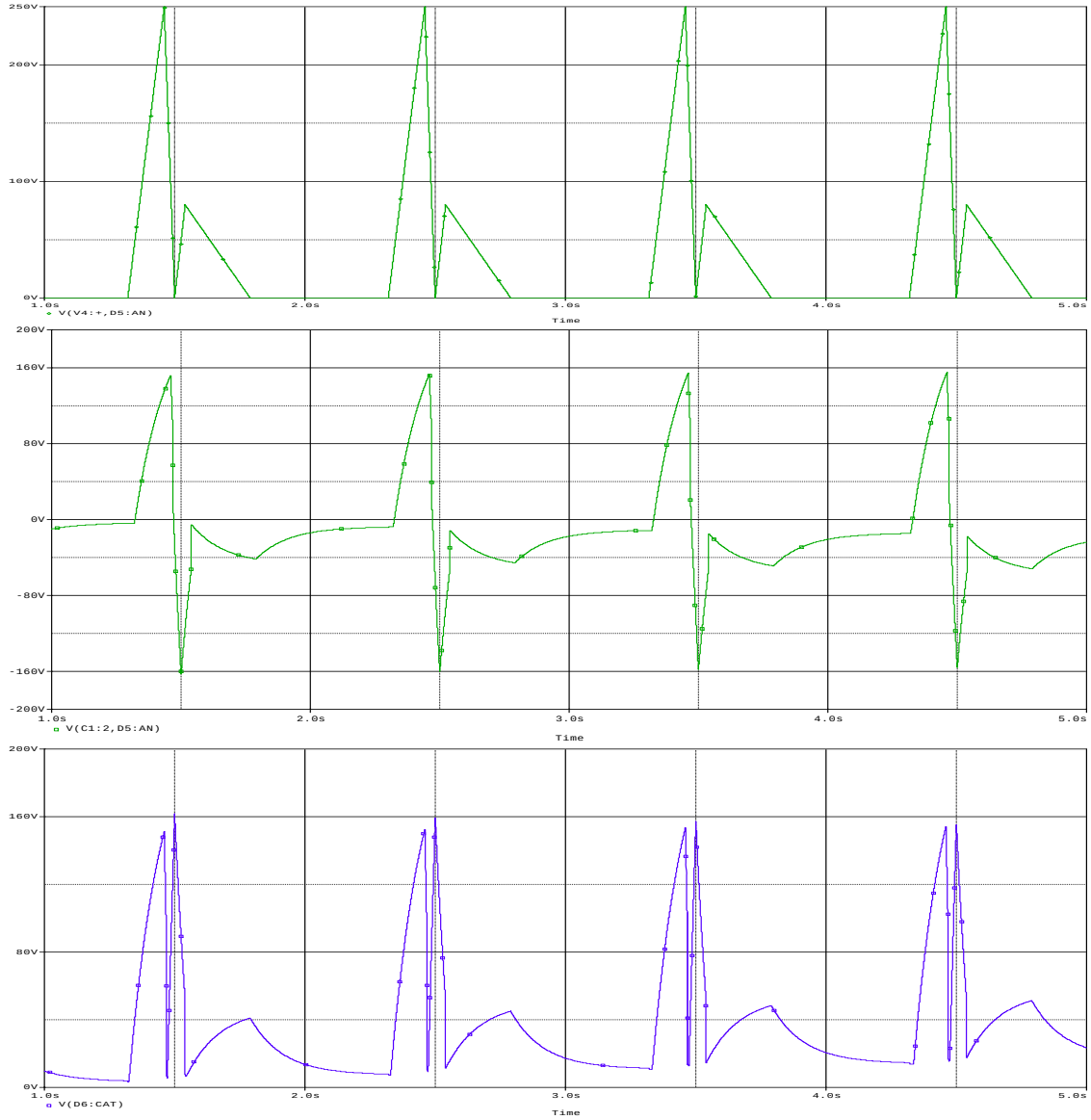


Figure 7.7: PSpice results from circuit in Figure 7.6, with original piezoelectric source signal (Top), equalized amplitude voltage source caused by intrinsic capacitance (Middle) the resulting rectified source signal as seen by the peak detection component of SSHI circuit.

This source response is actually advantageous for this project, since it allows the SSHI circuit to capture both possible peaks of the Piezo-element source, more energy can

be captured and stored. Furthermore, even though the output waveform is much different now, the SSHI circuit needs little change for peak detection and triggering. Both PVDF insole and PZT insole were tested to gather data points for the power vs. load resistance. The resulting curves are presented in Figure 7.8 and 7.9.

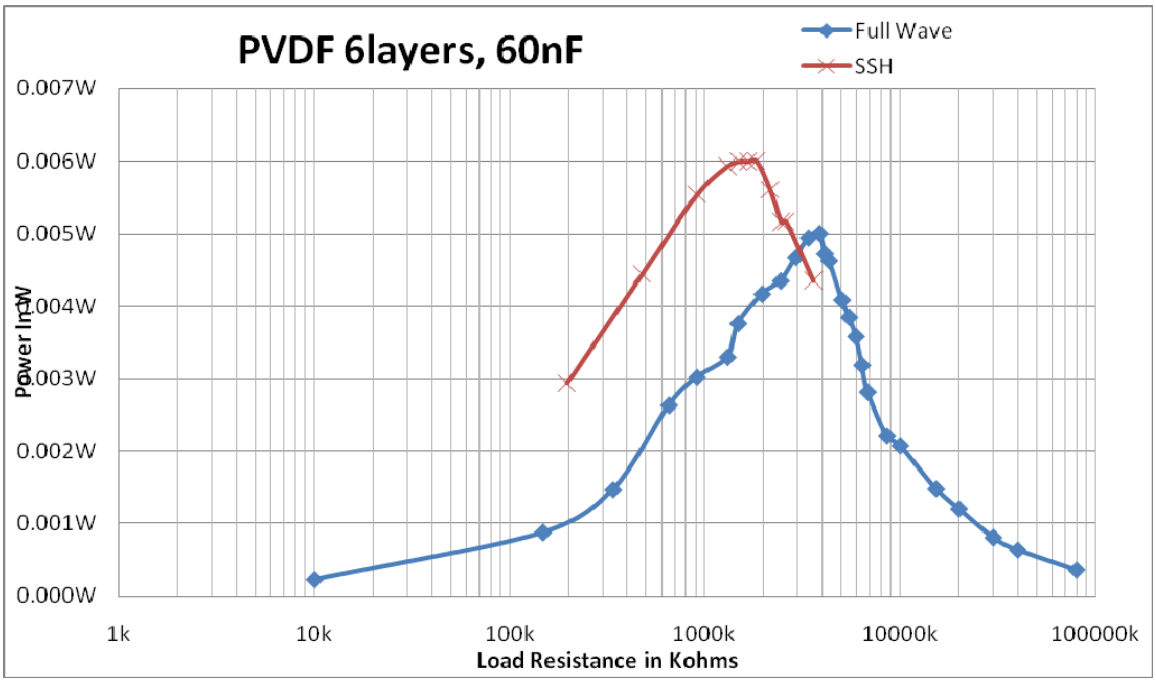


Figure 7.8: Power vs load resistance curve for SSHI circuit of PVDF insole, including converntial full-wave rectifier. The SSHI give ~19% moremaxmum ouput power than thant of converntial full-wave.

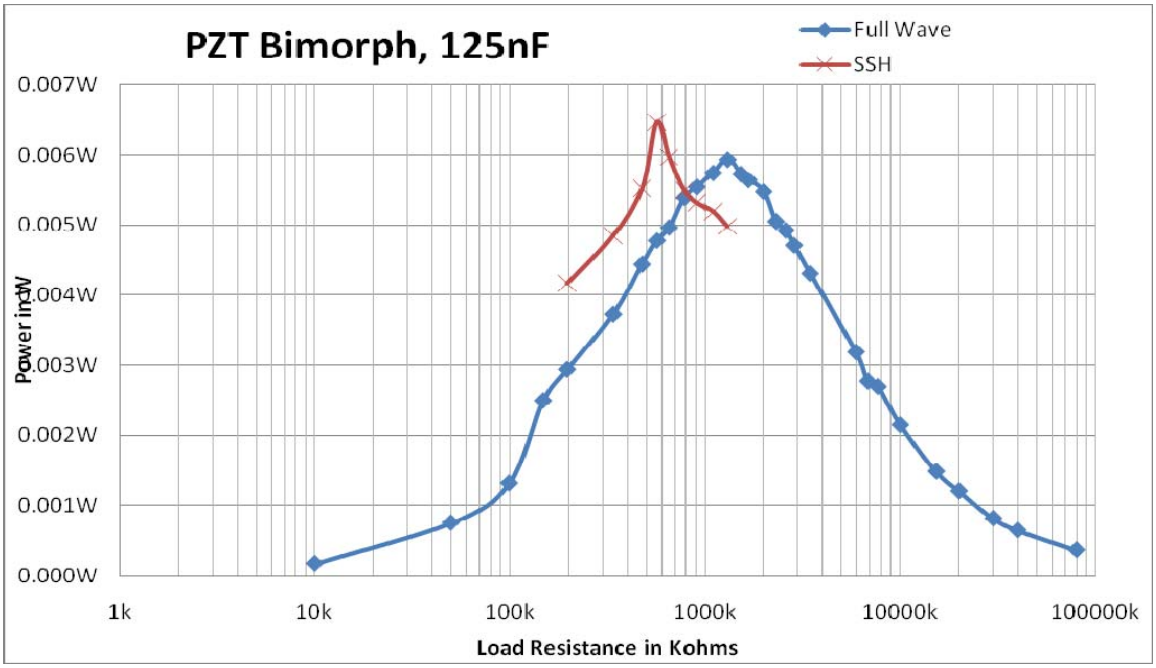

Figure 7.9: Power vs load resistance curve for SSHI circuit of PZT insert, including converntial full-wave rectifier. The SSHI give ~10% moremaxmum ouput power than thant of converntial full-wave.

As the power curves in Figure 7.8 and 7.9 displayed, the SSHI circuit did not perform as well as it did for the Robbins/Morris study. Under the SSHI circuit extraction, the PVDF insole obtained a maximum power of 6.04mW over a 1.836MΩ optimal load (compared to 5.0mW over 3.86MΩ with full-wave rectifier), while the PZT insole obtained a 6.64mW over a 566kΩ (compared to 5.94mW over 1.3MΩ with full-wave rectifier). The optimum load resistance of the SSHI circuit can be empirically derived (from pervious Robbins/Morris study attached in Appendix B), and shown here in Equation 7.1. Ts = 1, Cs = 125nF for PZT and 60nF for PVDF, L = 0.92H and R = 8Ω, Rs was calculated to be 3.74MΩ for PVDF insole and 1.80MΩ for PZT insert, just as experimental results have verified.

$$R_s = \frac{T_s}{4C_s}\left[\frac{1-e^{-\phi}}{1+e^{-\phi}}\right]$$ Equation 7.1

$$\text{Where } \phi = \frac{\pi}{2Q_s} \text{ and } Q_s = \frac{\omega L}{R}$$

The SSHI circuit only increases the maximum power output by ~10-20%, as oppose to 200%+ expected increase. One factor that caused the underwhelming performance of SSHI circuit is the inability to trigger the switch at the exact peak of the Piezo source. This is due to varying waveforms from each step taken, it is near impossible to calibrate each step exactly the same as the one before or after. Compounding this issue is the very narrow switch closing length, 1ms. The difference between the shoe energy harvester and the wind energy harvester is one consists of constant waveforms controlled by wind tunnels, while the other consists of static waveforms. In addition, for relatively identical source waveforms, the wind energy harvester system is stationary, allowing constant monitoring through oscilloscope and real time tweaking of SSHI circuit to insure proper peak acquisition. However, with the shoe harvester, it's near impossible to constantly monitor the wave form or any real time tweaking of SSHI circuit.

Although the inability to capture the peaks of Piezo source contributed to the poor SSHI circuit performance; the main reason appears to be the faulty modeling of piezoelectric source. Under the current model, the piezoelectric source is viewed an ideal, however experimental results from the SSHI circuit investigation have shown to be just the opposite. There exist many losses associated with the piezo source that has not been taken into account, especially mechanical conversion losses associated with stressing the piezoelectric materials during walking. A better model must be derived before another proper power extraction circuit can be designed and used to further increase harvestable energy. However, unfortunately, this task will have to be explored in future studies.

Finally, the PVDF insole and the PZT Thunder insert were combined together to determine the total power extractable by full-wave rectifier per shoe. Independent full-wave rectifiers are need to rectify the AC source, then both serial and parallel methods of connects were tested with and the resulting power curves are shown in the figure below.

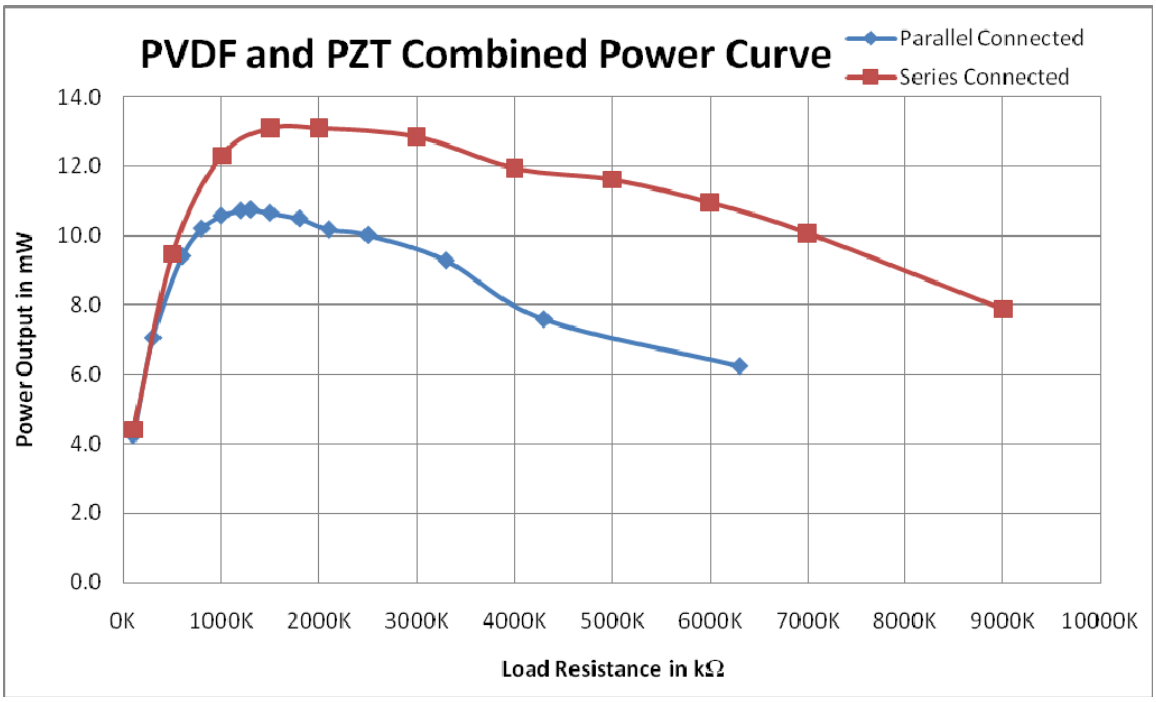


Figure 7.10: Combined Power Output from PVDF insole and PZT insole through series or parallel connections after independent rectifiers.

From Figure 7.9, the best result for this project come from combining the PVDF insole and the PZT insert through a series network after independent full-waver rectifiers. When connected in parallel, the combined maxmium power reaches 10.74mW over a 1.35MΩ load, which is just under the sum of maxmium power from independently recitifed and stored PVDF insole and PZT insert. The series combination yielded a 22% improvement over the parallel connected and independently collected, measurment at 13.1mW over a 2MΩ. Under sinusoide source conditions, the series combination power output should performed better at higher impedance due to lower capacitantce of series source capacitance combination (resluting in higher optimal load resistance), while

parallel combaintion should performed better at lower impedance due to higher capacitance of parallel source capacitance combination (resluting in lower optimal load resistance). However experimental and simulation results shows that series combiation perform better in lower load resistance than the cacluated optimal load resistance. The exact reason for this behavior is unclear, however it may have to do with the pulse nature of source waveforms, resulting in unexpected performance when compared with the familiar sinusoidal sources. As mentioned above and detailed in the next section, comprehesive modeling of these piezoelectric sources is required.

These results not only fulfill but clearly exceed the objective setout at the onset of this project: to reach 10mW over an optmized load with two pairs of Piezoelectric harvesting shoes. By combining an additional shoe, the ultimate power that could be harvested easly reach 20mW-26mW.

### 7.2 Recommendations for Future Work

Much as been done through this study to increase the energy extraction of piezoelectric materials from walking; however, there is still room for improvement. One obvious area that was already been mentioned is the better modeling of piezoelectric sources. The current model still views the Piezo-elements as ideal sources; however it is very clear from the experimental data that this is not the case. Efficiency calculations and

controlled studies on mechanical to electrical energy conversion for the piezo-shoe insert must be done in order to provide a solid source model and estimation of the mechanical loss involved within the system. With the better source modeling, a new energy extraction circuit, similar to the SSHI used in this report, needs to be designed and experimented with to further improve power output.

For the propulsive phase PVDF insole, other materials could be explored to increase flexibility while maintaining "structure memory". The current nylon variety, although very flexible after etching, becomes deformed or curved after extensive use. Other plastics or even metal could be examined for further improvement. Also, the adhesive used to bond PVDF sheets to the insole and each other is another aspect that needs further exploration. Although DP-105 has performed very well in experiments for this study, there are still countless adhesives on and off the market that may perform better with a thinner application and perhaps be cheaper.

For the PZT Thunder insert, the current design has performed exceptionally well by concentrating force toward the center of the pre-stressed curve for optimal energy extraction. However, one area yet to be explored is stacking multiple pieces of PZT Thunder on each side of the reverse clamshell construction: by having four Thunder pieces in the insert. This would easily double the energy density of contact phase insert,

minimally increasing the overall insert thickness since the Thunder pieces are already very thin.

Beyond the improvements aforementioned, another appropriate dimension to explore is the integration of a low-power, body-worn electronics to the system as the load. The MIT Media Laboratory has previously demonstrated a low range RFID transmitter using their PVDF insole system. Many other systems can be utilized in conjunction with the improved power output from this study. For example, a "quick look" GPS system can be easily integrated for military or recreational positioning, navigating or emergency applications. Another load could be a system of 3-axial accelerometers for activity or workout monitoring, much like the commercially available NIKE+ IPod connective divides. There is a myriad of other possibilities. With the ever increasing popularity of mobile electronics and ever decreasing power requirements for these electronics, many future body-worn devices could be powered by piezoelectric shoe energy harvesters.

# Bibliography

[1] Starner, T., “Human Powered Wearable Computing,” IBM Systems Journal, Vol. 35, No. 3&4, 1996, pp. 618-629

[2] Fletcher, R., “Force Transduction Materials for Human-Technology Interfaces” IBM Systems Journal, Vol. 35, No. 3&4, 1996, pp. 630-638

[3] Kymissis, J., Kendall, J., Paradiso, J. and Gershenfeld, N., “Parasitic Power Harvesting In Shoes,” Second IEEE International Conference on Wearable Computing (ISWC), October 1998

[4] “Walking Power Electronics,” Popular Mechanics, March 1999, pg 16.

[5] "Energy Scavenging with Shoe-Mounted Piezoelectric," Nathan S. Shenck, Joseph A. Paradiso. IEEE Micro, Vol. 21, No. 3, May-June 2001, pp. 30-42

[6] Geffrey K. Ottman, Heath F. Hoffman, Archin C. Bhatt, George A. Lesieutre, Adaptive Piezoelectric Energy Harvesting circuit for Wireless Remote Power Supply, IEEE Transactions on Power Electronics, Vol.17, No5, Sept. 2002

[7] William P. Robbins, Ian Marusic, Dustin Morris, Todd Novak, "Wind-Generated Electricity Using Flexible Piezoelectric Materials", International Symposium on Applications of Ferroelectrics (ISAF 2008), Santa Fe, NM, Feb. 24-27, 2008 (Invited paper)

[8] "Metalized Filmsheets Data Sheet", URL: http://www.meas-spec.com/piezo-film-sensors/piezo-film-sheets.aspx, Measurement Specialties Inc., 2010

[9] Dausch, D. and Wise, S., “Compositional Effects on Electromechanical Degradation of RAINBOW Actuators,” NASA, Hampton, Virginia, 1998

[10] "THUNDER TH-6R DATA SHEET", URL: http://216.71.30.251/Face%20International/6r-ds.pdf, Face International Corp., 2010

[11] "Macro Fiber Composite Data Sheet", URL: http://www.smart-material.com/media/Publications/MFC-brochure_2010_V3.1.pdf, Smart Material Corp., 2010

[12] "Piezo Stack Actuators Data Sheet", URL: http://www.americanpiezo.com/products_services/stack_actuators.html, American Piezo Ceramics Inc., 2010

# Appendix A

**Custom Inductor Design and Calculations of Robbins/Morris study.**

The design requirements for the inductor are low power dissipation and high inductance. Low power dissipation is necessary to achieve a high Q value and furthermore an efficient energy harvesting circuit. A large inductance value is desired for longer switch on time (Equation 5.9). A longer switch on time allows the switching transients to be more forgiving (longer $t_{rise}$, $t_{fall}$, and $t_{delay}$ times). Therefore, a ferrite core was chosen for the inductor design. Ferrites have high permeability which leads to a physically smaller inductor as well. The inductor must be able to support voltages as high as 150 V base to peak. The inductor must sustain a maximum current given by the peak voltage divided by the characteristic impedance. This maximum current (considering bimorph PVDF) is expressed in Equation 5.6, where $Z_o$ is the characteristic impedance of the LC network.

$$I_{peak} = \frac{V_{peak}}{Z_0} = \frac{V_{peak}}{\sqrt{L_r / C_r}} = \frac{150V}{\sqrt{.92H / 200nF}} \approx 70mA \qquad \text{(Equation 5.6)}$$

In the construction of the inductor, AWG 32 copper wire was wound around the ferrite core to achieve an inductance on the order of 1 H. The actual inductance value was found to be .92 H which is satisfactory for the SSSHI circuit design (the final one-shot on-time must be adjusted to half the resonant period of the LC network).

The switch is to be closed for half the period of the resonance between the capacitance of the PVDF and the inductor which is derived by Equations 5.7-5.9.

$$f_s = \frac{1}{2\pi\sqrt{L_r C_r}} \qquad \text{(Equation 5.7)}$$

$$T_s = \frac{1}{f_s} = 2\pi\sqrt{L_r C_r} \qquad \text{(Equation 5.8)}$$

$$T_{on} = \frac{T_s}{2} = \pi\sqrt{L_r C_r} \qquad \text{(Equation 5.9)}$$

The transistors used for the switch design have large breakdown voltages and hence larger depletion regions to withstand these voltages. When turning these devices on and off the charge must be pulled out of the depletion region. Because more charge must be pulled out of the device the switching time is increased. These high voltage devices are not going to provide fast, accurate switching for the SSSHI circuit, but if the on time of the switch is much greater than the time to turn the switch on and off, the power losses due to the slow switching will be minimized. The higher the resonating inductance of the closed switch LC network, the greater the on-time of the switch (Eq. 5.9), and hence the more forgiving the switching characteristics of the PMOS and NPN transistors are allowed to be. This was the motivation to use an inductance value on the order of 1 H. With $L_r$ = 1 H and $C_{pvdf}$ = 200 nF, $T_{on}$ is on the order of 1 ms which is much longer than the switching times ($t_{on} \sim t_{off} < 50$ μs) of the PMOS and NPN transistors used.

A relatively high saturation flux density is necessary to support 150V without core saturation, given a small cross-sectional area ferrite core. Core material 78 from Fair-Rite Corp. was chosen as the ferrite core. Having a relative permeability of 2500 and a saturation flux density of 480 mT, 78 Material™ was more than sufficient to meet the inductor design requirements. Fair-Rite's 75 Material™ was also explored due to its high permeability of 5000 and saturation flux density of 400 mT. A photograph of the inductor designed with 78 Material™ core is shown in **Figure 5.5**.

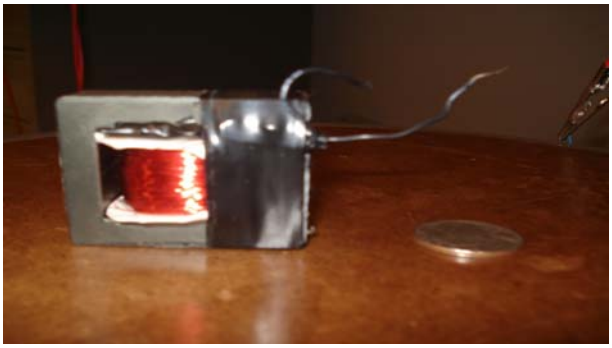

**Figure 5.5** *Photograph of .92 H inductor designed for low-power, high voltage energy harvesting circuit. Inductor has a Q value of 30, making it very efficient for the SSSHI circuit. A quarter is shown to give a sense of the inductor physical size.*

The inductor design specifications are expressed in Equations 5.10 – 5.11, where Vsat is the saturation voltage of the core, $\omega_0$ is the frequency multiplied by 2π, $B_{sat}$ is the saturation flux density of the core, and $A_c$ is the cross-sectional core area.

$$V_{sat} = \omega_0 N B_{sat} A_c \qquad \text{(Equation 5.10)}$$

Given $\omega_0 = 800\pi$ rad/s, N = 600 turns, $A_c = 2.37$ cm$^2$, and $B_{sat} = 480$ mT, Vsat is calculated in Equation 5.6.

$$V_{sat} = (400Hz)(2\pi)(600turns)(.48T)(.000237m^2) = 172V \qquad \text{(Equation 5.11)}$$

A core saturation voltage of 172 V is sufficient to withstand the MFC-PZT voltages as well as PVDF voltages. The saturation voltage was found to be approximately 180 V experimentally. The measured inductance was found to be .92 H. The series resistance is 10 Ω. The Q value of the inductor was found to be approximately 30 at the resonant frequency of the PVDF capacitance, inductance resonance. The resonant frequency is expressed in Equation 5.12.

$$f_o = \frac{\omega_o}{2\pi} = \frac{1}{2\pi}\left(\frac{1}{\sqrt{LC_{pvdf}}}\right) = \frac{1}{2\pi}\left(\frac{1}{\sqrt{(.92H)(200nF)}}\right) = 371Hz \qquad \text{(Equation 5.12)}$$

An inductor was also designed using Fair-Rite 75 Material™. This ferrite core has a relative permeability of 5000 and thus allows a physically smaller inductor size to reach an inductance on the order of 1 H.

The inductor was wound using AWG 32 copper wire. The measured series resistance was found to be 15 Ω. The calculated Q value is approximately 30 at 400 Hz. This core is very efficient when subjected to voltages less than 90 V ($V_{sat}$), which is sufficient for MFC-PZT ($d_{31}$-mode) piezoelements. However, the core saturates when using MFC-PZT ($d_{33}$-mode) or PVDF. The saturation voltage is expressed by Equation 5.13, which matches very close to experimental results.

$$V_{sat} = (400Hz)(2\pi)(600turns)(.40T)(.000137m^2) = 83V \qquad \text{(Equation 5.13)}$$

Both inductors designed for the SSSHI circuit have on-state losses proportional to their individual resistances. The DC resistance (DCR) of these inductors is on the order of 15-20 Ω. The power losses due to the DCR are, however trivial. Because the inductor and PVDF internal capacitance is resonating @ approximately 400 Hz (Equation 5.10), the AC resistance of the inductor must be calculated to give an

accurate description of how much power is being lost in the inductor winding. The AC resistance of both inductors was found empirically to be approximately 100 Ω at 1 kHz. Inductor AC resistance values were calculated by first measuring the bandwidth of resonance and determining the Q value each inductor. An approximate power loss due to the AC resistance of the inductor is expressed in Equation 5.14.

$$P_{R,ac} = \langle I^2 \rangle R_{ac} D = \left( \frac{(70mA)^2}{\pi} \right) (100\Omega) * 1\% = 1.56mW \qquad \text{(Equation 5.14)}$$

The inductor's winding resistance is the **critical path** of the SSSHI circuit design (besides that of the dielectric loss of the piezoelectric material). Meaning, it is the largest contributor to power loss of all components within the SSSHI circuit. A great deal of work was put into the design of the inductor for this very reason. The hysteresis and core losses of the inductor are trivial compared to the winding losses because a ferrite core is implemented in the inductor design.

# Appendix B

## Effective Source Resistance of Quasi-Resonant Rectifier

Under these conditions, the current i(t) is given by

$$i(t) \approx A\exp(-t/\tau)\sin(\omega_R t) \tag{B1}$$

Where $\tau = 2L/(R)$, $\omega_R = \omega_o\sqrt{1-(2Q_s)^{-2}}$ , $\omega_o = (LC_s)^{-1/2}$ and $Q_s = \omega_o L/R$. The charge $Q_{ex}$ extracted from the piezo element during this interval is

$$Q_{ex} = \int_0^{\pi/\omega_o} i(t)dt = \frac{A}{\omega_o}(1+e^{-\phi})\sqrt{1-\frac{1}{4Q_s^2}} \tag{B2}$$

Where $\Phi = \pi / (2Q_s)$. The charge $Q_{ex}$ replaces the charge drained from the storage capacitor C during the time interval $T_s/2$ ($T_s = 1/f_s$ where $f_s$ is the frequency of the flapping of the piezo element). The charge drawn from the storage capacitor is approximately given by

$$Q_{ex} = \frac{V_o T_s}{2R_L} \tag{B3}$$

And the constant 'A' in Eqs. (B1) and (B2) becomes

$$A = \frac{V_o T_s \omega_o}{2R_L(1+e^{-\phi})\sqrt{1-\frac{1}{4Q_s^2}}} \tag{B4}$$

During the time interval $T_{cl} \approx \pi/\omega_o$, the energy $E_s$ extracted from the piezo element is given by B5.

$$E_s = V_s Q_{ex} = \frac{V_s V_o T_s}{2R_L} \tag{B5}$$

This extracted energy is balanced by energy dissipation and energy storage in the rest of the circuit. Conservation of energy considerations yields

$$E_s = E_R + E_C \tag{B6}$$

Where $E_R$ is the energy dissipated in the inductor parasitic series resistance R (and on-state resistance of the switch) during the $T_{cl}$, and $E_C$ is the energy stored in the capacitor C and then dissipated in the load between re-charging intervals.

The energy $E_C$ is given by

$$E_C = \frac{V_o^2 T_s}{2R_L} \tag{B7}$$

The energy $E_R$ dissipated in the resistor R is given by

$$E_R = \int_0^{\pi/\omega_o} Ri^2(t)dt = \frac{V_o^2 T_s^2 (1-e^{-\phi})}{8C_s R_L^2 (1+e^{-\phi})} \tag{B8}$$

Using Eqs. (B5), (B7), (A-8) and (B8), the conservation of energy equation, Eq. (B6) becomes

$$\frac{V_s V_o T_s}{2R_L} = \frac{V_o^2 T_s^2 (1-e^{-\phi})}{8C_s R_L^2 (1+e^{-\phi})} + \frac{V_o^2 T_s}{2R_L} \tag{B9}$$

Simplifying Eq. (B9) yields

$$V_o = \frac{V_s}{(1+R_s/R_L)} \tag{B10}$$

$R_S$ is given by

$$R_s = \frac{T_s}{4C_s}\left[\frac{1-e^{-\phi}}{1+e^{-\phi}}\right] \tag{B11}$$